

See discussions, stats, and author profiles for this publication at: <https://www.researchgate.net/publication/263941196>

Understanding the Second-Order Nonlinear Optical Properties of One-Dimensional Ruthenium(II) Ammine Complexes

ARTICLE *in* THE JOURNAL OF PHYSICAL CHEMISTRY C · JANUARY 2013

Impact Factor: 4.77 · DOI: 10.1021/jp309309v

CITATIONS

15

READS

7

2 AUTHORS:



Yuexing Zhang

University of Massachusetts Amherst

67 PUBLICATIONS 1,362 CITATIONS

SEE PROFILE



Benoît Champagne

University of Namur

401 PUBLICATIONS 8,737 CITATIONS

SEE PROFILE

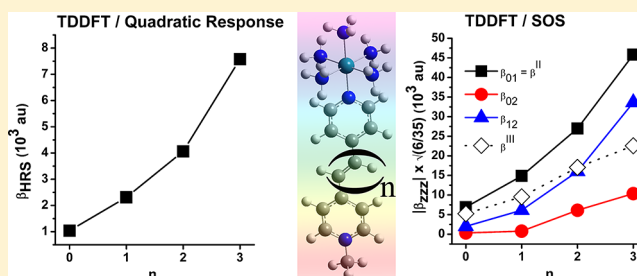
Understanding the Second-Order Nonlinear Optical Properties of One-Dimensional Ruthenium(II) Ammine Complexes

Yuxing Zhang and Benoît Champagne*

Laboratoire de Chimie Théorique (LCT), Unité de Chimie Physique Théorique et Structurale (UCPTS), University of Namur, rue de Bruxelles, 61, B-5000 Namur, Belgium

Supporting Information

ABSTRACT: First principles calculations of the linear and nonlinear optical properties are carried out for three series of one-dimensional ruthenium(II) ammine complexes with one pyridyl pyridinium ligand containing different numbers of C_2H_2 units or the $(CH=CH)-Ph-(CH=CH)$ linker. The substitution effects upon introducing one pyridine or one *N*-methylimidazole moiety as donor instead of ammonia have also been studied in detail. These calculations employing density functional theory with different exchange-correlation functionals as well as the polarizable continuum model approach to describe the solvent effects show that these compounds are challenging for theoretical chemistry and that their nonlinear optical responses are complex and depend on many structural and electronic factors. Two major types of methods have been employed to calculate and analyze the first hyperpolarizabilities (β): (i) the summation-over-states scheme, applied to calculate the longitudinal β tensor component, truncated to one or two dominant excited states, of which the results are compared to Stark spectroscopy data, and (ii) the quadratic response schemes, providing the whole second harmonic generation response of the compound, which can be compared to the values derived from hyper-Rayleigh scattering measurements. Using response theory calculations, off-resonant first hyperpolarizability values display a monotonic increase as a function of the number of C_2H_2 units (from 0 to 3 units, corresponding to compounds 1–4, respectively) in the pyridyl pyridinium ligand (in the three series with NH_3 , pyridine, and *N*-methylimidazole substituent in opposite position to the large ligand). These calculations, which evidence the dominance of the longitudinal β tensor component and a consistent depolarization ratio close to 5.0, also predict a smaller β value when the $(CH=CH)_3$ linker of the pyridyl pyridinium ligand (compound 4) is replaced by the $(CH=CH)-Ph-(CH=CH)$ linker (compound 5). To some extent, the calculations performed at a wavelength of 1064 nm confirm these trends, despite the presence of resonance enhancements. Calculations carried out within the summation-over-states scheme to analyze the origin of these β variations reproduce the monotonic increase of β in the 1–4 series, but compounds 4 and 5 are predicted to have similar β values. Upon relating these β variations to those of spectroscopic properties like the excitation energies, transition dipoles, and dipole moments of a pair of excited states (a low-energy metal to ligand charge transfer and a high-energy intraligand charge transfer excited state), the calculations point out the impact of including a second excited state in the treatment, since it leads to a decrease of β by about 50%. Though substituting the ammonia group by a pyridine has a limited impact on the linear and nonlinear optical properties of the complexes, the substitution by *N*-methylimidazole increases β by about 25%, which has been attributed to the contribution of *N*-methylimidazole to the HOMO and the subsequent bathochromic shifts of the excitation energies. In most of the cases, qualitative and even semiquantitative agreement is observed between theory and experiment, which enables one to get a deep insight into the structure/property relationships of these molecules. When this is not the case, we elaborate on the limitations of the methods of calculations and of the experimental treatments of the measured data.



I. INTRODUCTION

Due to the potential utility in novel optoelectronic and photonic technologies, molecular materials with large nonlinear optical (NLO) properties are of great interest and have been extensively investigated both experimentally and theoretically.¹ An increasing amount of research has shown that organometallic complexes of transition metals offer versatility for combining NLO effects with other characteristics, such as ultrafast response times, low dielectric constants, good processability as thin-film devices, and enhanced nonresonant

responses in view of producing novel multifunctional materials.² Besides, organometallic compounds also show advantages over traditional organic molecules owing to their strong UV/vis absorption bands (metal-to-ligand charge transfer and ligand-to-metal charge transfer), their redox properties, and the tuning effect of the metal on the electronic

Received: September 19, 2012

Revised: December 19, 2012

Published: December 24, 2012

properties of the organic fragments.³ As a result, organometallic structures are intriguing second-order NLO chromophores. Nevertheless, the study of their NLO properties is currently less mature in comparison to the purely organic materials, which have been scrutinized very extensively.

Among these organometallic compounds, ruthenium complexes with ammonia and pyridyl pyridinium groups are typical compounds exhibiting very large first hyperpolarizabilities (β). Coe and co-workers have designed and synthesized a broad range of ruthenium complexes, having one-dimensional,⁴ two-dimensional,⁵ and also three-dimensional⁶ structures. These compounds have been structurally, optically, and electrochemically characterized allowing the deduction of structure–property relationships. Moreover, the second-order NLO properties of these complexes have been thoroughly studied using hyper-Rayleigh scattering (HRS) and Stark spectroscopy (electronic absorption, SS) measurements. Large β_0 (static or intrinsic first hyperpolarizability) responses have been deduced and attributed to the strong metal-to-ligand charge transfer (MLCT) excited state. In addition, they have shown that the MLCT absorption is highly tunable and can be readily and reversibly switched via the Ru^{II/III} redox couple,⁷ which leads to modifications of their NLO properties. The two-state approximation (TSA), which associates β with optical spectroscopic properties, was found useful to interpret these results.

In order to analyze the NLO responses and subsequently to design new NLO-phores, quantum chemistry characterizations are complementary and provide insights into the interplay between the structural, electronic, and optical properties of these transition metal compounds. In the case of Ru^{II}-based electron donor–electron acceptor (D–A) compounds, a few theoretical studies have analyzed their second-order NLO responses. Most of these employ density functional theory (DFT) and time-dependent DFT (TDDFT) approaches. By resorting to B3P86/LANL2DZ calculations, Coe et al.^{4k} have qualitatively described the experimentally observed trends of the Stark-derived static β of complexes 1–4 and (1-py)–(4-py) (Figure 1) and have found that the finite field (FF) molecular first hyperpolarizability does not increase steadily with increasing length of the π spacer but reaches a maximum for compounds 3 and 3-py and then decreases when going toward 4 and 4-py. This behavior was analyzed within the TSA using excitation energies (ΔE_{0n}), transition dipole moments (μ_{0n}), and ground (μ_0) and excited state (μ_n) dipole moments, since the TSA β is proportional to $\mu_{0n}^2 (\mu_n - \mu_0) / \Delta E_{0n}^2$. Though within this approximation and level of calculation the static β increases monotonically in both series with the ligand size, their calculations have pointed out a decrease of $(\mu_n - \mu_0)$ between 3 and 4 (and also between 3-py and 4-py) that might explain the experimental trend. A similar DFT/B3P86 approach was subsequently used by Coe and collaborators to investigate other one-dimensional and also two-dimensional complexes. Inerbaev and co-workers⁸ adopted also the TDDFT/B3P86 method to investigate the ground and excited state properties of ruthenium(II) ammine complexes 1–4 (Figure 1) both *in vacuo* and in solvent. Their TDDFT/B3P86 study has highlighted (i) the key role of the solvent, which red-shifts the absorption energy maxima and enhances the polarizations in the ground and excited states, (ii) the impact of the geometry—and the method to determine it—on the optical properties, (iii) the fact that the best agreement between experimental and theoretical excitation energies is achieved

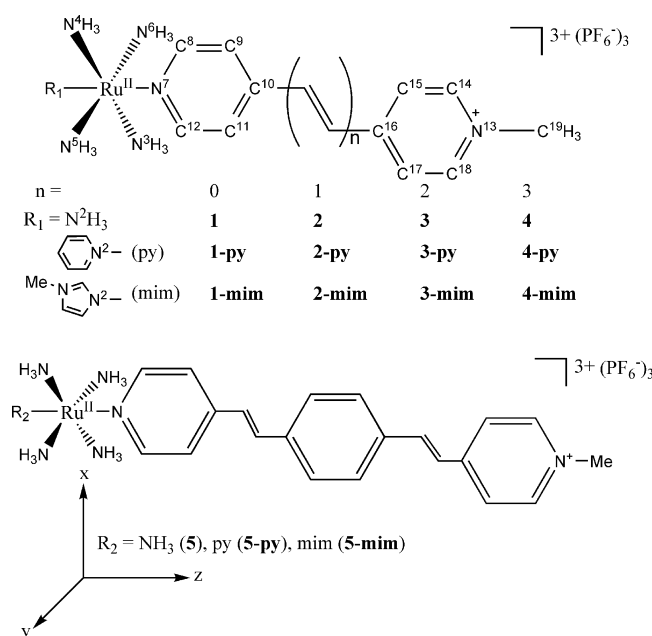


Figure 1. Chemical structures and atomic labeling (in superscript) of the cations. py = pyridine, mim = N-methylimidazole. The axes convention used in the theoretical calculations is also shown.

when the geometries are optimized at the Hartree–Fock level, (iv) despite a severe overestimation, a reproduction of the experimental evolution of $\Delta\mu_{0n} = (\mu_n - \mu_0)$, the change of dipole moment between the ground and first dominant excited state, which increases as a function of the size of the linker, and (v) the monotonic increase of the TSA static β with the linker size, which deviates from the experimentally observed trend^{4k} and, therefore, which raises questions about the contribution of the other excited states as well as about its frequency dispersion.

In the present paper, in view of further understanding the second-order NLO properties of Ru(II) ammine complexes, we carry out DFT and TDDFT calculations to investigate the geometries, electronic structures, excited state properties, and NLO responses of three series of Ru(II) ammine complexes with one pyridyl pyridinium ligand containing different numbers of C_2H_2 units or the $(CH=CH)-Ph-(CH=CH)$ linker (**n**, **n-py**, and **n-mim** with **n** = 1–5, Figure 1). Major issues encompass (i) the analysis of the evolution of the linear and nonlinear optical properties as a function of the number of ethylenic units in the ligand, (ii) the comparison between the $(CH=CH)_n$ and $(CH=CH-Ph-CH=CH)$ linkers, and (iii) the effect of introducing pyridine (py) and N-methylimidazole (mim) groups as a donor instead of ammonia. These structure–property issues are accompanied by an analysis of the performances of different methods and levels of calculations: DFT and TDDFT with different XC functionals, the time-dependent Hartree–Fock (TDHF) method to calculate the first hyperpolarizabilities, and the polarizable continuum model (PCM) to describe the effects of the solvent. β results include the TSA, its extension including a second excited state, as well as (implicit all-state) response theory calculations. This allows making comparisons with both experimental HRS and SS results. Our paper is organized as follows: after describing the essentials of the theoretical methods (section II), the results on the geometries, electronic structures, and linear and nonlinear optical properties are

presented and discussed in section III. Section IV extends the discussion and provides a general conclusion.

II. THEORETICAL AND COMPUTATIONAL ASPECTS

The ground state molecular structures were optimized using DFT calculations with the B3P86 hybrid exchange–correlation (XC) functional⁹ along with the LANL2DZ basis set,¹⁰ which includes an effective core potential (ECP) for Ru and the 6-31G* basis set for the other atoms. No symmetry constraint was imposed during geometry optimization. The B3P86 functional was proved to be the most accurate XC functional for describing the geometries of the Ru^{II} ammine complexes among a list including B3LYP,¹¹ PBE,¹² BLYP,^{11b,13} BPW91,^{13a,14} TPSS,¹⁵ M06, and M06L.¹⁶ Moreover, the LANL2DZ/6-31G* basis set combination for (Ru)/(C, N, and H) atoms gave more accurate results than the uniform use of the LANL2DZ basis set.¹⁷ The ground state geometries of the 1–4 complexes were also optimized in acetonitrile (MeCN) solvent using the integral equation formalism variant (IEF) of PCM.¹⁸ At the optimized structures, harmonic vibrational frequencies (all real) were calculated to confirm that all optimized structures correspond to energy minima.

UV/visible absorption spectra of the complexes were simulated on the basis of excitation energies and oscillator strengths evaluated with the time-dependent DFT (TDDFT) method and the IEFPCM scheme (solvent = MeCN). 40 singlet excited states were evaluated in these calculations, carried out on the geometries optimized *in vacuo* with the B3P86/(LANL2DZ, 6-31G*) method. A similar level of theory has already been employed to study a broad range of organometallic compounds and has been shown to be efficient.¹⁹ Gaussian functions with a halfwidth of 2000 cm^{−1} were used to simulate the absorption spectra. For comparison, the UV/visible absorption spectra of 1–4 were also calculated with the B3LYP,¹¹ M06,¹⁶ M06-2X,²⁰ PBE0,^{12,21} and LC-BLYP²² XC functionals. The electron density difference between the ground and the *n*th excited states, $\Delta\rho_n(\vec{r})$, was calculated from molecular orbital electron densities according to the formula

$$\begin{aligned}\Delta\rho_n(\vec{r}) &= \rho_n(\vec{r}) - \rho_0(\vec{r}) \\ &= \sum_i^{\text{occ}} \sum_a^{\text{unocc}} f_{n,i \rightarrow a}(\vec{r}) \\ &= \frac{\sum_i^{\text{occ}} \sum_a^{\text{unocc}} c_{n,i \rightarrow a}^2 [\rho_a(\vec{r}) - \rho_i(\vec{r})]}{\sum_i^{\text{occ}} \sum_a^{\text{unocc}} c_{n,i \rightarrow a}^2}\end{aligned}\quad (1)$$

where $c_{n,i \rightarrow a}$ is the expansion coefficient corresponding to the promotion of an electron from the occupied ϕ_i to the unoccupied ϕ_a Kohn–Sham orbital in the *n*th TDDFT excited state wave function and $\rho_{i/a}(\vec{r}) = |\phi_{i/a}(\vec{r})|^2$. The electron density difference between the ground and excited states consists thus in a linear combination of various one-electron transition densities. Only singly excited configurations whose coefficient squares are larger than 5.0% of the sum of all the coefficient squares were taken into account. The geometries of the dominant excited states were also optimized, using the TD-B3P86 XC functional, the LANL2DZ/6-31G* basis set, and the IEFPCM scheme.

Two types of approaches were employed to calculate the first hyperpolarizabilities: (i) response theory and (ii) perturbation theory methods. On the one hand, the time-dependent

Hartree–Fock (TDHF)²³ and the coupled-perturbed Hartree–Fock (CPHF) schemes were applied—using the geometries optimized *in vacuo*—to obtain the dynamic ($\lambda = 1064$ and 1900 nm) and the static first hyperpolarizabilities, respectively. The TDDFT approach²⁴ with different XC functionals including B3P86,⁹ M06,¹⁶ M06-2X,²⁰ and LC-BLYP²² was also applied to obtain the dynamic and static first hyperpolarizabilities. Solvent effects were described using the IEFPCM scheme.^{18,25} Another mixed basis set was employed: the 6-31+G* basis set for the C, N, and H atoms combined with LANL2DZ for Ru atoms was used, since it is well suited to describe the hyperpolarization phenomena. However, including this set of s and p diffuse functions is not expected to have a large impact on the β of large D/A systems, contrary to that of small molecules.

On the other hand, the perturbation theory approach was also used in order to unravel the relationships between the optical spectroscopic properties and the first hyperpolarizabilities. This approach, which leads to summation-over-states (SOS) expressions of β , was adopted only for the diagonal β_{zzz} tensor component [*z* is directed along the longitudinal or intramolecular charge-transfer (ICT) direction, Figure 1] that is dominant in one-dimensional push–pull π -conjugated systems. First, within the two-state approximation (TSA) introduced by Oudar and Chemla,²⁶ the static first hyperpolarizability is determined by a low-energy (often the first) ICT excited state and reads

$$\beta_{zzz,0}^{\text{TSA}} = \beta_0^{\text{II}} = \beta^{\text{II}} = 3 \frac{\Delta\mu_{01}(\mu_{01})^2}{(\Delta E_{01})^2} \quad (2)$$

The $\Delta\mu_{01}$ values were calculated from FF calculations of the TDDFT/B3P86 excitation energies using the following expression generalized to any *n*th excited state:

$$\begin{aligned}\Delta E_{0n}(F_z) &= \Delta E_{0n}(0) - (\mu_{n,z} - \mu_{0,z})F_z \\ &\quad - \frac{1}{2}(\alpha_{n,zz} - \alpha_{0,zz})F_z^2 - \dots\end{aligned}\quad (3)$$

and therefore

$$\Delta\mu_{0n,z} = (\mu_{n,z} - \mu_{0,z}) = \frac{\Delta E_{0n}(F_z) - \Delta E_{0n}(-F_z)}{-2F_z} - 0(F_z^2) \quad (4)$$

As shown in Table S1 in the Supporting Information, the combination of ± 0.0005 and ± 0.0010 au field amplitudes with one Romberg iteration leads to numerical stability of ~ 0.2 D or better. In addition, the excited state dipole moments were also computed at the TDDFT level from the population analysis using the CI density and the $\Delta\mu_{0n}$ values were calculated as the differences with respect to the ground state values. Both the equilibrium and non-equilibrium solvation models were employed.

In a second step, to improve over the TSA and because all complexes show a second strong absorption band at smaller wavelengths (*vide supra*), the three-state approximation (3SA) was employed and the first hyperpolarizability expression becomes

Table 1. Selected Bond Lengths (Å) and Dihedral Angles (deg) Optimized with the B3P86 XC Functional and the LANL2DZ (Ru Atom)/6-31G* (C, N, and H Atoms) Basis Set in Vacuum (Vac) and in Acetonitrile Solvent (Sol)

	Exp ^a	1		1-py		1-mim		2		3		4		4-py	4-mim	5	5-mim
		Vac	Sol	Vac	Vac	Vac	Sol	Vac	Sol	Vac	Sol	Vac	Sol	Vac	Vac	Vac	Vac
Ru ^I –N ²	2.167 ^b	2.187	2.165	2.123	2.116	2.191	2.165	2.193	2.165	2.194	2.165	2.125	2.121	2.196	2.123		
Ru ^I –N ³	2.137	2.174	2.154	2.166	2.165	2.170	2.154	2.169	2.153	2.168	2.154	2.163	2.163	2.167	2.161		
Ru ^I –N ⁴	2.146	2.172	2.153	2.166	2.165	2.172	2.154	2.170	2.151	2.168	2.152	2.163	2.162	2.170	2.163		
Ru ^I –N ⁵	2.161 ^b	2.174	2.153	2.167	2.164	2.172	2.155	2.169	2.154	2.168	2.154	2.163	2.163	2.169	2.163		
Ru ^I –N ⁶	2.040 ^c	2.173	2.153	2.167	2.166	2.169	2.151	2.170	2.154	2.168	2.153	2.163	2.162	2.168	2.161		
Ru ^I –N ⁷	2.048 ^c	2.114	2.064	2.133	2.123	2.111	2.068	2.111	2.074	2.111	2.077	2.126	2.120	2.108	2.118		
N ⁷ –C ⁸	1.359 ^d	1.352	1.352	1.351	1.352	1.352	1.352	1.352	1.352	1.353	1.352	1.352	1.352	1.353	1.352		
C ⁸ –C ⁹	1.365 ^d	1.387	1.383	1.387	1.387	1.385	1.383	1.383	1.383	1.381	1.382	1.382	1.382	1.381	1.382		
C ⁹ –C ¹⁰	1.388 ^d	1.400	1.400	1.401	1.401	1.404	1.402	1.407	1.404	1.409	1.405	1.408	1.408	1.409	1.408		
C ¹⁰ –C ¹¹	1.388 ^d	1.401	1.400	1.401	1.401	1.405	1.405	1.408	1.405	1.410	1.406	1.409	1.409	1.410	1.409		
C ¹¹ –C ¹²	1.376 ^d	1.387	1.383	1.387	1.387	1.384	1.380	1.382	1.380	1.381	1.381	1.381	1.381	1.380	1.380		
C ¹² –N ⁷	1.356 ^d	1.352	1.352	1.351	1.351	1.355	1.355	1.355	1.355	1.356	1.355	1.354	1.354	1.356	1.354		
N ¹³ –C ¹⁴	1.341 ^d	1.350	1.350	1.349	1.350	1.353	1.354	1.353	1.354	1.354	1.355	1.354	1.355	1.355	1.354		
C ¹⁴ –C ¹⁵	1.381 ^d	1.381	1.376	1.382	1.381	1.377	1.373	1.375	1.372	1.374	1.371	1.374	1.374	1.373	1.373		
C ¹⁵ –C ¹⁶	1.373 ^d	1.403	1.404	1.402	1.403	1.407	1.409	1.409	1.412	1.411	1.413	1.411	1.412	1.412	1.412		
C ¹⁶ –C ¹⁷	1.393 ^d	1.401	1.402	1.403	1.403	1.405	1.406	1.407	1.408	1.409	1.410	1.410	1.410	1.410	1.410		
C ¹⁷ –C ¹⁸	1.383 ^d	1.383	1.378	1.381	1.381	1.38	1.377	1.378	1.375	1.377	1.374	1.376	1.376	1.376	1.375		
C ¹⁸ –N ¹³	1.340 ^d	1.348	1.348	1.350	1.349	1.348	1.349	1.350	1.350	1.351	1.351	1.351	1.351	1.351	1.351		
N ¹³ –C ¹⁹	1.488 ^d	1.481	1.471	1.480	1.480	1.477	1.470	1.475	1.469	1.474	1.468	1.473	1.473	1.473	1.472		
C ¹⁰ –C ¹⁶	1.494 ^d	1.481	1.470	1.480	1.479	3.873	3.849	6.313	6.288	8.759	8.736	8.759	8.759	10.503	10.504		
average single	1.494 ^d	1.481	1.470	1.480	1.479	1.461	1.452	1.449	1.443	1.441	1.437	1.441	1.441	1.429	1.429		
average double						1.349	1.351	1.356	1.357	1.360	1.360	1.360	1.359	1.369	1.368		
BLA						0.112	0.101	0.093	0.086	0.081	0.078	0.081	0.081	0.061	0.061		
C ⁹ –C ¹⁰ –C ¹⁶ –C ¹⁵	51.2/27.0	37.7	31.3	35.1	34.7	10.8	1.4	−0.9	1.1	1.2	3.8	1.3	1.1	4.9	9.1		

^aSelected bond length (Å) and dihedral angles in the crystal of *cis*-[Ru^{II}(NH₃)₄(MeQ⁺)₂][PF₆]₄ reported in ref 5c. ^bBond length between Ru and the nitrogen atom of ammonia opposite to the pyridyl pyridinium. ^cBond length between Ru and the nitrogen atom of the pyridyl pyridinium ligand. ^dBond lengths in the MeQ⁺ unit with a dihedral angle of 51.2°.

$$\beta_{zzz,0}^{3SA} = \beta_0^{\text{III}} = \beta^{\text{III}} = \frac{3\Delta\mu_{01}(\mu_{01})^2}{(\Delta E_{01})^2} + \frac{3\Delta\mu_{02}(\mu_{02})^2}{(\Delta E_{02})^2} + \frac{6\mu_{01}\mu_{12}\mu_{02}}{(\Delta E_{01})(\Delta E_{02})} = \beta_{01} + \beta_{02} + \beta_{12} \quad (5)$$

The two first terms (β_{01} and β_{02}) are the traditional diagonal contributions to β , associated with the first and second excited states, whereas the third one is an off-diagonal term involving interactions between these two states and the ground state. Since the TDDFT method does not provide the transition dipole moments between excited states, the μ_{12} values were calculated by adopting the Thomas–Kuhn sum rules including the first three states (the ground and two excited states) and solving the $(m, p) = (0, 1)$ equation.²⁷ This approach was employed recently to model the frequency dispersion of β of an amphiphilic porphyrin chromophore by integrating spectroscopic data from the experimental linear absorption spectrum together with β values at selected frequencies.²⁸

In the case of the TDDFT and TDHF calculations, all the β tensor components were evaluated and we focused on the second-harmonic generation (SHG) response for which the $\beta(-2\omega; \omega, \omega)$ tensor contains 18 independent elements. In particular, the quantities under study are related to the HRS experiments²⁹ with nonpolarized incident laser light and observation of plane-polarized scattered light made perpendicular to the propagation plane. Assuming an incident light propagating along the *X* direction and a scattered light at 90°

along the *Y* direction and vertically polarized along the *Z* axis, β_{HRS} reads

$$\beta_{\text{HRS}}(-2\omega; \omega, \omega) = \beta_{\text{HRS}} = \sqrt{\langle \beta_{zzz}^2 \rangle + \langle \beta_{zxx}^2 \rangle} \quad (6)$$

The depolarization ratio, DR, which reveals the shape of the NLO-phore, is given by

$$\text{DR} = \frac{I_{\text{VV}}^{2\omega}}{I_{\text{HV}}^{2\omega}} = \frac{\langle \beta_{zzz}^2 \rangle}{\langle \beta_{zxx}^2 \rangle} \quad (7)$$

where $\langle \beta_{zzz}^2 \rangle$ and $\langle \beta_{zxx}^2 \rangle$ are orientational averages of all the β tensor components in the molecular frame, which are proportional to the scattered signal for vertically and horizontally plane-polarized incident signals, respectively. These orientational averages were evaluated following the approach employed in recent studies.³⁰ In addition, we focused on the longitudinal β_{zzz} tensor component, that dominates the β tensor.

To define β , the B convention³¹ was used throughout the whole work. All calculations were performed by using the Gaussian 09 program.³²

III. RESULTS AND DISCUSSION

III.A. Geometries. Figure 1 shows the chemical structures and the atomic labeling of the complexes, while their key optimized structure parameters are listed in Table 1. A number of remarkable structural features are observed. The two pyridine rings of **1** are not coplanar but form a dihedral angle (C⁹–C¹⁰–C¹⁶–C¹⁵) of 37.7°, in agreement with the result of Inerbaev et al.⁸ but different from the imposed C_s symmetry

structures of Coe et al.^{4k} Additional calculations on **1** constraining the symmetry to C_s lead to two imaginary frequencies of $48i\text{ cm}^{-1}$ or larger, indicating that the C_s isomer of **1** is a transition state instead of a minimum. The Ru–N²(NH₃) bond in **1** (2.187 Å) is longer than the other four (almost equatorial) Ru–N^{3–6}(NH₃) bonds (2.172–2.174 Å), but all the Ru–N(NH₃) bonds are longer than the Ru–N⁷(pyridyl pyridinium ligand) bond (2.114 Å) due to backbonding in the latter. The amplitude ordering among the calculated Ru–N bond lengths matches well the trend found in the *cis*-[Ru^{II}(NH₃)₄(MeQ⁺)₂][PF₆]₄ crystal,^{5c} i.e., Ru–N(ligand) \ll Ru–N(NH₃) < Ru–N²(NH₃). This trend is in agreement with the results of Inerbaev et al.⁸ at the B3P86 and MP2 levels. Note that according to the latter results⁸ the MP2 method seems to overestimate the Ru–N bonds more significantly than the B3P86 XC functional, substantiating the reliability of B3P86 to describe the geometries of Ru complexes. On the other hand, ref 8 has showed that the HF method provides the opposite trend, i.e., Ru–N(ligand) > Ru–N(NH₃), to the X-ray diffraction data on the related *cis*-[Ru^{II}(NH₃)₄(MeQ⁺)₂][PF₆]₄ compound.

Along with the increase of the π -conjugation length from **1** to **5**, the Ru–N²(NH₃) bond length increases to 2.194 Å in **4** and to 2.196 Å in **5**, while the Ru–N^{3–6}(NH₃) bond decreases to 2.168 and 2.167–2.170 Å in **4** and **5**, respectively. Meanwhile, the Ru–N⁷(ligand) bond length decreases from 2.114 Å in **1** to 2.111 Å in **2–4** and to 2.108 Å in **5**. These results indicate that lengthening the π -conjugated segment strengthens slightly the Ru–N⁷(pyridyl pyridinium ligand) coordination bond and the four Ru–N^{3–6}(NH₃) bonds perpendicular to Ru–N⁷ bond but it slightly weakens the Ru–N²(NH₃) bond. These variations in $d_{\text{Ru–N}}$ can be related to the decrease of the bond length alternation (BLA) of the polyenic segment between the pyridine and pyridinium rings, from 0.112 Å in **2** to 0.081 and 0.061 Å in **4** and **5**, which corresponds to stronger π -electron delocalization and charge transfer effects. More precisely, the average single bond length on the conjugation groups between C¹⁰ and C¹⁶ decreases from 1.461 Å in **2** to 1.441 and 1.429 Å in **4** and **5**, while the average double-bond length increases from 1.349 Å in **2** to 1.360 and 1.369 Å in **4** and **5**, respectively. Considering the major relationship between BLA and β , one expects an increase of β upon going from **1** to **5**. In addition, owing to the increased distance between the two rings and the reduction of the inter-ring repulsions, with respect to **1**, the dihedral angle between the two pyridine rings is significantly reduced in **2–5** and reaches almost zero, favoring also a better conjugation between the two pyridine rings and, in principle, an increased β value. At the same time, the N⁷–C⁸, N⁷–C¹², C⁹–C¹⁰, and C¹⁰–C¹¹ bond lengths in the pyridine ring coordinating the Ru atom increase a little, while the C⁸–C⁹ and C¹¹–C¹² bond lengths decrease in the same order. The bond changes in the terminal pyridine ring follow the same trend as those in the coordinating pyridine ring. The N¹³–C¹⁹(Me) bond also decreases from 1.481 Å in **1** to 1.474 and 1.473 Å in **4** and **5**. The geometrical trends also agree with those observed by Inerbaev et al.⁸ at the B3P86 and MP2 levels of approximation.

When pyridine and *N*-methylimidazole donor groups are introduced on the position opposite to the pyridyl pyridinium ligand—and therefore replace an ammonia moiety—the molecular structures change to some extent but the trends remain the same as in the NH₃-substituted complexes **1–5**. In particular, the Ru–N²(py) bond in **1-py** is about 0.064 Å

shorter than the Ru–N²(NH₃) bond in **1**, the Ru–N^{3–6}(NH₃) bonds decrease by 0.006–0.008 Å, and the Ru–N⁷(ligand) bond increases by 0.019 Å. Comparing the geometry of **1-py** with **4-py** shows that the Ru–N²(py) bond increases slightly from 2.123 Å in the former to 2.125 Å in the latter, while the Ru–N^{3–6}(NH₃) bonds decrease from 2.166 to 2.167 to 2.163 Å and the Ru–N⁷(ligand) bond decreases from 2.133 to 2.126 Å. A similar analysis can be made when NH₃ is replaced by the *N*-methylimidazole (mim) unit. In comparison with py-substituted complexes (**1-py** to **5-py**), the Ru–N² bond and the Ru–N^{3–6}(NH₃) bonds in **1-mim** to **5-mim** are further shortened due to the stronger electron-donating ability of mim. However, the amplitude of the Ru–N⁷(ligand) bond increase in mim-substituted complexes is smaller than that in the py-substituted complexes.

The solvent effects were then assessed by comparing the optimized molecular structures of **1–4** *in vacuo* with those performed with IEFPCM (solvent = MeCN). With the exception of the N¹³–C¹⁴, N¹³–C¹⁸, C¹⁵–C¹⁶, and C¹⁶–C¹⁷ bonds, solvent effects lead to a shortening of the other bonds. The Ru–N bonds change more significantly than the other ones: the largest Ru–N bond shortening upon solvation is as large as 0.050 Å and the smallest is still 0.014 Å, while the variations of the other bond lengths is less than 0.010 Å. These results indicate that the polarized coordination bonds are more influenced by a polar solvent like MeCN than the covalent bonds in the pyridyl pyridinium ligand. In addition, in the polyenic segment, the average single-bond length decreases while the average double-bond length increases, resulting in a BLA decrease. Moreover, the evolution of the geometrical parameters as a function of the ligand size is almost the same as *in vacuo*, indicating that the influences of the solvent on the geometry and on the π -conjugation are small. As a result, most of the following linear and nonlinear optical properties calculations are based on the optimized structure *in vacuo*, but to further substantiate this choice, for selected cases, the properties were also calculated using the optimized structure in MeCN.

III.B. Electronic Structures. Figure 2 displays the MO energy diagrams as determined at the B3P86/(LANL2DZ, 6-31G*) level using the IEFPCM scheme (solvent = MeCN) on the ground state geometries optimized *in vacuo*. The main observations are as follows: (i) both the HOMO and LUMO energies increase from **1** to **5** with the size of the ligand (except for the LUMO of **1** which is higher than that of **2–4**), as also found for the ligand alone and for the complexes substituted with the py or mim group; (ii) the HOMO-3 of **2–5** (HOMO-4 for **1**) (the electronic transitions from these orbitals to the LUMO provide the main contributions to the second excited state as discussed later) also moves toward higher energy with the ligand size and tends to reach a limiting value; (iii) for complexes with a given ligand, both the HOMO and LUMO levels shift upward when substituting NH₃ by mim (except for **1**) but downward when substituting by py, indicating the mim > NH₃ > py electron-donating ordering; (iv) the substitution effect of the py and mim groups on the HOMO is much larger than on the LUMO and HOMO-3 (HOMO-4 for **1**); (v) the HOMO–LUMO gap as well as the gap between HOMO-3 (HOMO-4 for **1**) and LUMO decrease from **1** (**1-py**, **1-mim**) to **4** (**4-py**, **4-mim**) with the number of double bonds in the linker [the HOMO–LUMO gap of **5** (**5-py**, **5-mim**) lies between those of **2** (**2-py**, **2-mim**) and **3** (**3-py**, **3-mim**)], while the (HOMO-3)–LUMO gap of **5** (**5-py**, **5-mim**) lies between

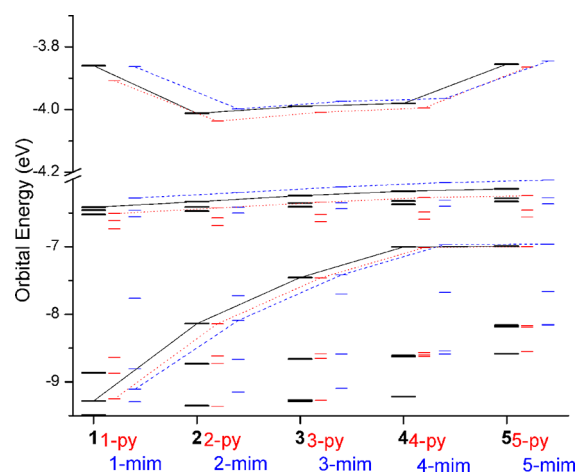


Figure 2. Molecular orbital energy levels of the complexes calculated at the B3P86/(LANL2DZ, 6-31G*) level using the IEFPCM scheme (solvent = MeCN) on the ground state geometries optimized *in vacuo*. Lines are drawn to connect the HOMO-3 (HOMO-4 for **1** and **2-mim** and HOMO-5 for **1-py** and **1-mim**), HOMO, and LUMO energy levels.

those of **3** (**3-py**, **3-mim**) and **4** (**4-py**, **4-mim**), figuring out the dependence of the first excitation energy with the conjugation length.

The main MOs involved in the dominant bands of the UV/visible absorption spectra of the Ru complexes are sketched in Figure 3. The HOMO of **1** is mainly described by the d orbital of Ru (86.5%) with some contributions from the π orbitals of the py ring connected with Ru. Going from **1** to **4**, the HOMO gets more delocalized on the ligand, inducing a decrease of the orbital composition on the Ru atom. In the HOMO of **4** and **5**, the orbital composition on the Ru atom attains 77.4 and 78.8%, respectively, indicating that the HOMO in these two complexes is still metal-based though the contribution of the ligand cannot be neglected. In contrast, the LUMOs in all five complexes are delocalized over the whole ligand with very little contribution from the Ru orbitals. On the contrary, the contribution of the HOMO-3 (HOMO-4 for **1**) to Ru increases from **1** to **4** and then decreases slightly to **5**. However, the largest contribution of Ru orbitals to the HOMO-3 is only 10.0% for **4**, indicating the ligand-based nature of these orbitals.

When R_1 = py or mim, the py and mim groups make contributions to the HOMO but they do not influence the LUMO, nor the low-lying occupied orbitals (HOMO-3, HOMO-4, or HOMO-5) of **2** (**2-py**, **2-mim**) to **5** (**5-py**, **5-mim**). This explains why the substitution of NH_3 by py and mim changes more the HOMO than the LUMO and the low-lying orbitals. In **1-py** and **1-mim**, the py and mim groups present a large contribution to the HOMO-5. The Ru content of the HOMO is larger by about 5% when R_1 = NH_3 than when R_1 = py or mim due to the orbital shift toward the py or mim groups. The same effect is observed for the HOMO-3 (HOMO-4, HOMO-5), in particular for the mim substituents. Nevertheless, the substitution by py and mim groups does not change the character of the HOMO, LUMO, and HOMO-X, neither their variations as a function of the ligand size.

III.C. Optical Absorption Spectra and Excitation Energies. Figure 4 displays the simulated optical absorption spectra of the complexes at the TDDFT/B3P86 level of approximation and Table 2 gives the nature of the electronic transitions together with sketches of the changes of the electron

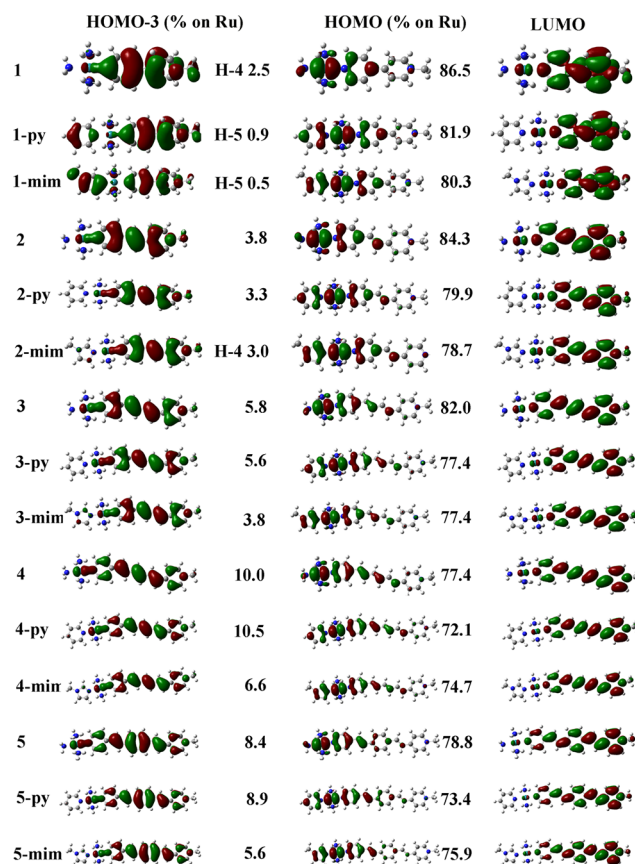


Figure 3. Selected frontier orbitals of the complexes calculated at the B3P86/(LANL2DZ, 6-31G*) level of approximation using the IEFPCM scheme (solvent = MeCN) on ground state geometries optimized *in vacuo*. Orbital maps were obtained with an isovalue of 0.02 au H-4 and H-5 are written when the corresponding orbitals are HOMO-4 and HOMO-5, respectively.

density upon excitation. The spectrum of compound **1** presents a band of medium intensity at 546 nm and a sharper one at 251 nm, which correspond to the electronic transitions from the HOMO to the LUMO and from the HOMO-4 to the LUMO, respectively. Both the orbital maps (Figure 3) and the electron density difference maps (Table 2) support the metal to ligand charge transfer (MLCT) nature of the lowest energy band at 546 nm. The amount of MLCT character of this transition can be estimated by the percentage of orbital distribution on the Ru atom in the HOMO (calculated as the sum of the squares of the LCAO coefficients on the Ru atom divided by the sum of the squares of all LCAO coefficients; eq 1). Since 86.5% of the HOMO is distributed on the Ru atom, the band at 546 nm is mainly a MLCT band. In contrast, the band at 251 nm is mostly intraligand charge transfer (ILCT) (over 97%) with small MLCT character due to the small Ru orbital contribution to the HOMO-4 orbital.

Along with the increase of the π -conjugated linker from **1** to **4**, the two absorption bands at 546 and 251 nm in **1** shift to 620 and 433 nm in **4**, respectively, but for both bands, this red shift saturates as a function of the ligand size. The larger red shift of the low-wavelength band with respect to the high-wavelength band is explained by its dominant HOMO-3 (or HOMO-4) to LUMO character and by the larger upward shift of this HOMO-3 with the ligand size with respect to the other involved frontier orbitals (Figure 2). Moreover, owing to the

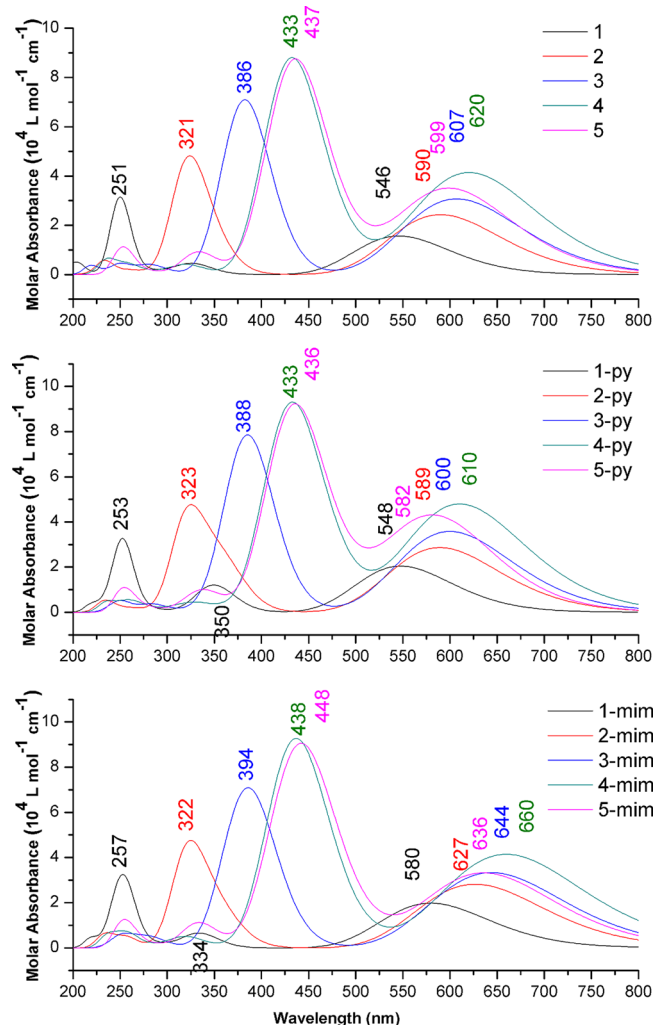


Figure 4. UV/vis absorption spectra of the three series of complexes simulated using Gaussian functions with a halfwidth of 2000 cm^{-1} together with TDDFT/B3P86 excitation energies and oscillator strengths.

delocalization of the HOMO on the py ring coordinating the Ru atom, the low-energy transition also displays some interligand charge transfer character for the longest members of the series. In addition, the percentage of MLCT in the lowest energy band decreases from 86.5% in **1** to only 77.4% in **4** and to 78.8% in **5**, supporting the decrease of MLCT character. In contrast, following the increase of Ru content of the HOMO-X ($X = 3, 4$, or 5), the percentage of ILCT in the high-energy band slightly decreases to the detriment of the MLCT character. Though the ligand is longer in **5** than **4** (2 ethylenes and 1 benzene ring with respect to 3 ethylenes), the lowest energy band in **5** appears at 599 nm, only at the red side of **2** containing only one ethylene unit. On the other hand, the second absorption band of **5** (437 nm) appears at the red side of **4** (433 nm). The oscillator strengths of both transitions increase as a function of the ligand size, but the high-energy transition possesses a larger oscillator strength.

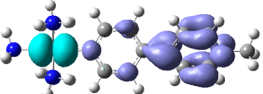
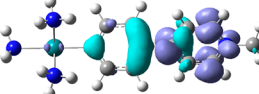
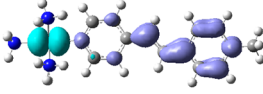
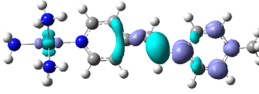
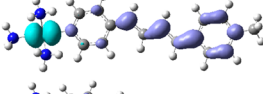
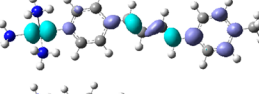
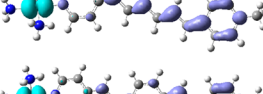
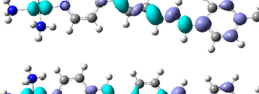
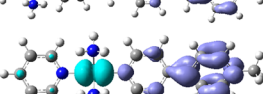
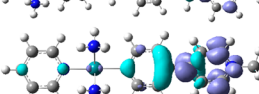
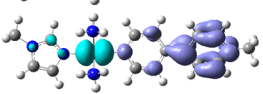
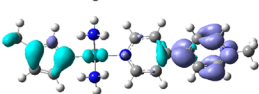
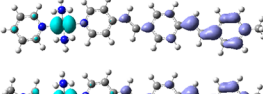
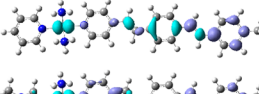
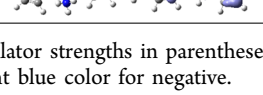
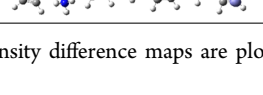
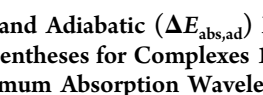
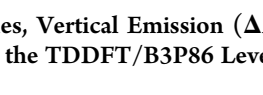
In the presence of the electron-donating py and mim groups, the electronic absorption bands of the complexes are shifted due to the modifications in the MO energies involved in the transitions. The lowest energy band of **1–5** shifts from 546, 590, 607, 620, and 599 nm to 548, 589, 600, 610, and 582 nm

in the py substituted complexes and to 580, 627, 644, 660, and 636 nm in the mim substituted complexes, respectively. Thus, in the mim-substituted complexes, this band is significantly red-shifted with respect to the nonsubstituted complexes **1–5**, while in most of the py-substituted complexes it is slightly blue-shifted. This result is in line with the HOMO and LUMO energy gap of the corresponding complexes. The high-energy bands in **1–5** are also red-shifted in the presence of the mim substituent, whereas the effect of the py substituent is almost negligible. Despite that, the substituent effects have a rather minor impact on the variation of the molar absorbance as a function of the ligand size, though for the low-energy band they lead to a rather systematic increase of the oscillator strength (Table S2, Supporting Information).

Table 3 lists the TDDFT/B3P86 vertical and adiabatic excitation energies as well as the vertical emission energies for the two lowest-energy transitions of the **1–4** complexes. The vertical excitation energies of **1–4** evaluated for (ground state) geometries optimized accounting for the solvent (MeCN) effects are also given, but the differences are negligible and always smaller than 7 nm. This is in line with the small structural changes when accounting for solvent effects, and this substantiates the use of optimized molecular structures *in vacuo* for predicting the electronic absorption spectra. In order to calculate the adiabatic excitation energies as well as the emission energies—though, experimentally, no emissive behavior has been reported to date—the geometrical structures of the excited states corresponding to the main absorption bands of **1–4** were optimized at the TDDFT level with the IEFPCM scheme to account for the solvent (MeCN), with the equilibrium solvation model. Upon transition to the first excited state, the Ru–N² bond is shortened by 0.035–0.048 Å, with the other Ru–N(NH₃) bonds being less shortened (by 0.011–0.020 Å), while the Ru–N⁷(ligand) bond is significantly lengthened by 0.102–0.185 Å in the first excited states for complex **1–3** (Table S3, Supporting Information). This is in line with the dominant MLCT character of the first excited state in **1–3**. Due to its increasing ILCT character, the geometry of the first excited state of **4** differs less from that of the ground state than in complexes **1–3**, with the shortening of the Ru–N² and the lengthening of Ru–N⁷(ligand) bonds attaining only 0.028 and 0.065 Å, respectively. In parallel with the charge transfer from the Ru atom to the ligand, the single bond lengths of the polyenic segment decrease, the double bond lengths increase, leading to a decrease of BLA (from 0.101, 0.086, and 0.078 Å for **2–4** to 0.066, 0.049, and 0.038 Å, respectively) and therefore to a stronger π -electron delocalization. In the case of **1**, the first excited state geometry is characterized by a larger CC double bond character of the C¹⁰–C¹⁶ bond, i.e., a smaller bond length going in pair with a reduction of the interring dihedral angle by 14°. The change of the dihedral angle upon excitation is much smaller in **2–4**, since it was already close to zero in the ground state.

For the second major transition, owing to its dominant ILCT nature, the Ru–N^{2–6} bonds of **1** are shortened by less than 0.005 Å and the Ru–N⁷(ligand) bond is lengthened by 0.098 Å, but the geometrical changes are much larger in the ligand. The same situation is found in complexes **2–4**. In comparison to the ground state, the BLA in the second excited state of **2–4** decreases more significantly than in the first one so that it reaches values as low as 0.011, 0.005, and 0.014 Å, respectively. Similarly to the first excited state, upon excitation, the double bond character of C¹⁰–C¹⁶ in **1** increases ($d = 1.430\text{ Å}$, dihedral

Table 2. Electronic Transition Nature and Electron Density Difference Maps for Selected Complexes as Determined at the TDDFT/B3P86 Level of Approximation Using the IEFPCM Scheme (Solvent = MeCN) on Ground State Geometries Optimized *in Vacuo*^b

	Low-energy band		High-energy band	
	ΔE (f) ^a Main transitions	Charge density difference	ΔE (f) ^a Main transitions	Charge density difference
1	546 (0.29) H→L(100%)		251 (0.53) H-4→L(100%)	
2	590 (0.45) H→L(100%)		321 (0.73) H-3→L(87.3%)	
3	607 (0.57) H→L(100%)		386 (1.12) H-3→L(63.8%) H→L+1(36.2%)	
4	620 (0.76) H→L(100%)		433 (1.62) H-3→L(91.4%) H→L+1(8.6%)	
5	599 (0.64) H→L(100%)		437 (1.52) H-3→L(67.0%) H→L+1(33.0%)	
1-py	548 (0.37) H→L(96.5%)		253 (0.54) H-5→L(100%)	
1-mim	580 (0.36) H→L(97.8%)		257 (0.40) H-5→L(77.5%) H→L+4(13.1%) H-6→L(6.7%)	
5-py	582 (0.79) H→L		436 (1.67) H-3→L(73.9%) H→L+1(26.1%)	
5-mim	636 (0.61) H→L		448 (1.27) H→L+1(63.8%) H-3→L(36.2%)	

^aVertical transition energies (in nm) and oscillator strengths in parentheses. ^bThe electron density difference maps are plotted using isovalues of 0.002 au. Gray blue color for positive and light blue color for negative.

Table 3. Calculated Vertical ($\Delta E_{\text{abs,vert}}$) and Adiabatic ($\Delta E_{\text{abs,ad}}$) Excitation Energies, Vertical Emission ($\Delta E_{\text{em,vert}}$) Energies as Well as Their Oscillator Strengths in Parentheses for Complexes 1–4 Calculated at the TDDFT/B3P86 Level of Approximation in Comparison with Experimental Maximum Absorption Wavelengths^a

	Exp. ^b	Theor.						
	ΔE_{max} (nm/eV)	$\Delta E_{\text{abs,vert}}$ (nm/eV) (f)	$\Delta E'_{\text{abs,vert}}$ ^c (nm) (f)	$\Delta E_{\text{abs,ad}}$ (nm)/(eV)	$\Delta E_{\text{em,vert}}$ (nm/eV) (f)	$E_{\text{r,ES}}$ ^d (eV)	$E_{\text{r,GS}}$ ^e (eV)	$E_{\text{r,ES}} + E_{\text{r,GS}}$ (eV)
1	590/2.10	546/2.27 (0.29)	539 (0.36)	613/2.02	687/1.80 (0.31)	0.25	0.22	0.47
	268/4.63	251/4.94 (0.53)	254 (0.51)	281/4.42	296/4.19 (0.53)	0.53	0.22	0.75
2	595/2.08	590/2.10 (0.45)	585 (0.53)	655/1.89	708/1.75 (0.47)	0.21	0.14	0.35
	312/3.97	321/3.86 (0.73)	320 (0.48)	364/3.40	391/3.17 (0.90)	0.46	0.24	0.69
3	584/2.12	607/2.04 (0.57)	607 (0.64)	673/1.84	718/1.73 (0.69)	0.20	0.12	0.32
	354/3.50	386/3.21 (1.12)	386 (1.13)	429/2.89	458/2.71 (1.18)	0.32	0.18	0.50
4	568/2.18	620/2.00 (0.76)	624 (0.82)	692/1.79	732/1.69 (1.11)	0.21	0.10	0.31
	392/3.16	433/2.86 (1.62)	432 (1.57)	490/2.53	522/2.38 (1.32)	0.33	0.16	0.49

^aRelaxation energies for the ground and excited states are provided in the last three columns. ^bReferences 4j and 4k in MeCN solution. ^cUsing geometrical structures optimized by accounting for solvent effects (MeCN). ^dRelaxation energy of the corresponding excited state, $E_{\text{r,ES}} = \Delta E_{\text{abs,vert}} - \Delta E_{\text{abs,ad}}$. ^eRelaxation energy in the ground state, $E_{\text{r,GS}} = \Delta E_{\text{em,ad}} - \Delta E_{\text{em,vert}}$ (NB: $\Delta E_{\text{em,ad}} = \Delta E_{\text{abs,ad}}$).

angle = 4.9°). For both the first and second excited states, the average bond length variations relative to the ground state generally decrease with the ligand size.

The calculated adiabatic excitation energies and vertical emission energies display the same trend as the vertical excitation energies, i.e., both excitation energies decrease with increasing ligand size from **1** to **4**. Using vertical and adiabatic excitation energies, the relaxation energies E_{r} in the ground,

first, and second excited states were calculated, evidencing the decrease and saturation of E_{r} from **1** to **4**. The total relaxation energy ($E_{\text{r,total}}$) is the sum of the relaxation energies of the ground ($E_{\text{r,GS}}$) and excited ($E_{\text{r,ES}}$) states, and it describes the redshift of the emission peak with respect to the absorption peak, known as the Stokes shift. For both the first and second excited states, $E_{\text{r,total}}$ decreases from **1** to **4**, in line with the distribution of the geometrical relaxation on the whole ligand

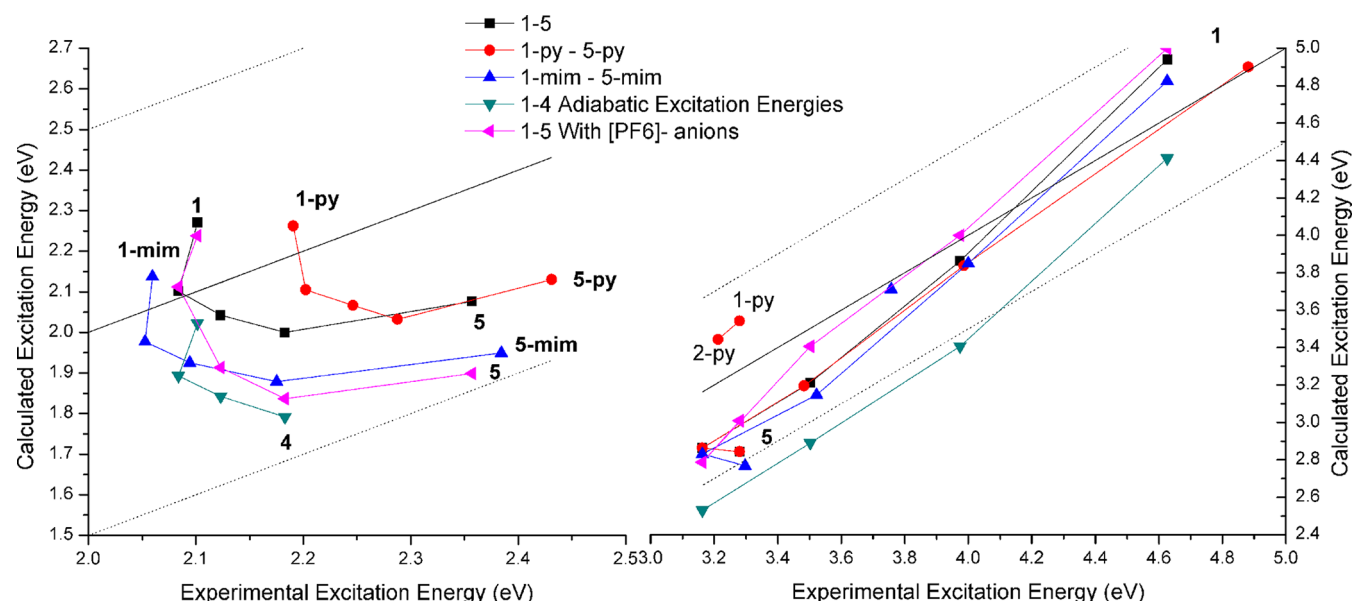


Figure 5. Comparison between the experimental and calculated excitation energies for the different complexes (left, low-energy band; right, high-energy band). The black solid line is $y = x$, and the two dotted lines above and below it correspond to the $y = x + 0.5$ and $y = x - 0.5$ relationships, respectively. The two red circles in the right figure labeled with **1-py** and **2-py** correspond to weak bands or band shoulders between the low- and high-energy bands of **1-py** and **2-py**, respectively.

and smaller bond length changes between the ground and excited states. In summary, the bands in both the UV/vis absorption and emission spectra shift to the red from **1** to **4**.

We now turn to the comparison with experiment. The calculated excitation energies of the second absorption band reproduce closely the experimental trend. On the other hand, for the low-energy band, the observed shift of the maximum absorption as a function of the ligand size differs from the calculated shift of both the vertical and adiabatic excitation energies. Still, these TDDFT/B3P86 excitation energies of compounds **1–4** match well other theoretical results.⁸ To assess whether $[\text{PF}_6]^-$ anions surrounding the complexes modify this trend, we reoptimized the structures of **1–5** *in vacuo* by introducing three $[\text{PF}_6]^-$ around the complex and then we calculated their excitation energies in MeCN solvent with the IEFPCM model using the same functional and basis set as for complexes without the surrounding $[\text{PF}_6]^-$ anions. This situation should be considered as extreme, since the model systems favor short distances between the charged species, but it will be indicative of the changes of trend that can be expected. As can be seen from Table S4 (Supporting Information), the inclusion of the $[\text{PF}_6]^-$ anions indeed changes the geometrical structures and shifts the absorption bands. For example, in **4**, the Ru–N² and Ru–N⁷(ligand) bonds decrease to 2.152 and 2.065 Å, respectively, in the presence of $[\text{PF}_6]^-$ anions and the lowest-energy band shifts from 620 to 675 nm. However, the evolution of the lowest-energy band as a function of the ligand size is the same with and without $[\text{PF}_6]^-$ anions, demonstrating a persisting difference between theory and experiment.

Figure 5 compares the calculated and experimental excitation energies for the investigated complexes. As can be seen, the calculated high-energy bands generally correlate well with the experimental ones. The calculations however overestimate the excitation energy of **1**, **1-py**, and **1-mim** but underestimate those of other complexes, especially of **5**, **5-py**, and **5-mim**. The largest difference between the calculated and experimental excitation energies is 0.53 eV for **5-mim**, and the smallest is

only 0.02 eV for **1-py** with an average absolute difference as small as 0.28 eV. In contrast, the agreement between theory and experiment is qualitatively less good for the low-energy band. For example, experimentally, the excitation energies globally increase slightly with the size of the ligand and follow the trend $2 < 1 < 3 < 4 < 5$, whereas theoretically the ordering is almost reverse with a decrease of the excitation energy when lengthening the polyenic segment: $4 < 3 < 5 < 2 < 1$. This is probably due to the shortcomings of TDDFT in calculating the excitation energies of charge-transfer (CT) excited states; i.e., long-range and multireference effects are partly or not described.³³ Note that a brief assessment of the former effect by using XC functionals with different amounts of long-range HF exchange (LC-BLYP and M06-2X) does not bring improvement with respect to the trends as a function of ligand size (Table S5, Supporting Information). Moreover, the B3LYP and M06 XC functionals predict the correct order for the excitation energies of compounds **3** and **4** but the overall ΔE variations are too large within the whole set of compounds. It is further interesting to mention that, adopting a similar TDDFT/B3P86 level of approximation, ref 4k predicts similar excitation energies for the low-energy band of compounds **1** and **2**. Thus, part of the overestimation of the excitation energies of **1** might originate from a too large inter-ring torsion angle or at least from motion around it. Thus, the bathochromic shift amounts to 0.04 and 0.20 eV for the low- and high-energy excitation energies of **1**, as we observed by performing additional calculations on the system with 0° torsion angle between the rings, which is therefore not sufficient.

Despite this, the calculated excitation energy trends for **1–5** are very similar to those of **1-py–5-py** and **1-mim–5-mim**, and the largest difference between theory and experiment for the lowest energy band is 0.43 eV for **5-mim** and the smallest is only 0.02 eV for **2** with an average absolute difference of only 0.18 eV. Moreover, the calculated adiabatic excitation energies of **1–4** and the calculated excitation energies of **1–5** with $[\text{PF}_6]^-$ anions display almost the same trends as the calculated

Table 4. Calculated Dipole Moment of the Ground, First, and Second Excited States Using Different Methods as Determined with the IEFPCM Scheme (Solvent = MeCN) and the B3P86 XC Functional

	μ_0^a	finite field ^b		CI density ^c		CI density ^d		CI density ^e		Exp. ^f	
		μ_1	μ_2	μ_1	μ_2	μ_1	μ_2	μ_1	μ_2	$\Delta\mu_1$	$\Delta\mu_2$
1	−2.30	−17.82	−7.32	−17.96	−7.48	−18.66	−7.25	−18.94 (−16.64)	−6.43	13.8	
2	−4.50	−22.51	−10.01	−22.80	−11.01	−23.68	−14.22	−24.93 (−20.43)	−9.36	16.2	
3	−6.85	−30.56	−18.48	−31.10	−19.01	−31.51	−14.75	−31.64 (−24.79)	−12.94 (−6.09)	22.4	12.7
4	−9.85	−38.39	−20.66	−39.38	−20.46	−39.18	−19.83	−37.01 (−27.16)	−18.28 (−8.43)	27.1	14.5
5	−14.01	−54.64	−32.60	−56.46	−33.74	−54.95	−31.29	−52.91 (−38.90)	−28.30 (−14.29)	28.3	13.6

^aIEFPCM calculations on IEFPCM optimized geometries. ^bCalculated with $\mu_n = \Delta\mu_{0n} + \mu_0$ ($n = 1, 2$), where the $\Delta\mu_{0n}$ values were calculated from FF calculations using the TD-B3P86/(LANL2DZ, 6-31G*) method based on the ground state geometry optimized in MeCN and non-equilibrium solvation model for the excited state. ^cCalculated using the non-equilibrium solvation model for the excited state based on the ground state geometry optimized in MeCN solvent. ^dCalculated using the equilibrium solvation model for the excited state based on the ground state geometry optimized in MeCN. ^eCalculated using the optimized excited state geometry in MeCN solvent and the equilibrium solvation model for the excited state. In parentheses are given the corresponding $\Delta\mu_{0n} = \mu_n - \mu_0$ ($n = 1, 2$) values to compare with experiment, in which the μ_0 values are those of column 2. ^fStark spectroscopic data taken from refs 4g, 4j, and 4k.

Table 5. Two and Three State Approximations to the Static Longitudinal (z) First Hyperpolarizabilities (in 100 au) of Compounds 1–5 as Determined from TDDFT/B3P86 Spectroscopic Quantities [Excitation Energies of States n , ΔE_{0n} , in eV; Transition Dipole Moments between States n and m , μ_{nm} , in D; Differences of Dipole Moments between States n and the Ground State, $\Delta\mu_{0n} = \mu_n - \mu_0$, in D]^a

	ΔE_{01}	ΔE_{02}	μ_0	μ_{01}	μ_{02}	μ_{12}^b	$\Delta\mu_{01}^c$	$\Delta\mu_{02}^c$	$\beta_{01} = \beta^{II}$	β_{02}	β_{12}	β^{III}
1	2.30	4.89	−2.30	6.46	5.25	5.93	−15.65	−5.17	−167	−8	48	−127
1 _{Exp} ^d	2.10	4.63		5.2			13.8		139			
2	2.12	3.88	−4.50	8.08	5.69	9.77	−18.30	−6.51	−359	−19	148	−230
2 _{Exp} ^d	2.08	3.97		5.5			16.2		203			
3	2.04	3.21	−6.85	9.11	9.62	10.71	−24.24	−12.16	−651	−147	387	−412
3 _{Exp} ^d	2.12	3.50		7.9	6.8		22.4	12.7	558	74		
4	1.99	2.87	−9.85	10.46	11.98	13.66	−29.53	−10.61	−1107	−250	812	−545
4 _{Exp} ^d	2.18	3.16		7.2	7.4		27.1	14.5	550	117		
5	2.05	2.84	−14.01	9.04	11.96	18.15	−42.45	−19.73	−1112	−473	909	−675
5 _{Exp} ^d	2.36	3.28		6.8	8.6		28.3	13.6	432	131		

^aThe calculations were performed using the IEFPCM scheme (solvent = MeCN) on molecular structures optimized at the DFT/B3P86 level in MeCN. ^bCalculated using the truncated Thomas–Kuhn sum rules. ^cDipole moment differences between the ground and excited states, in which the excited state dipole moments were computed at the TDDFT level using the CI density and the non-equilibrium solvation model. ^dStark spectroscopic data taken from refs 4g, 4j, and 4k, in which μ_{0n} is calculated from the oscillator strength f_{0n} according to $|\mu_{0n}| = [f_{0n}/(1.08 \times 10^{-5} \Delta E_{0n,max})]^{1/2}$, where $\Delta E_{0n,max}$ is the energy of maximum absorption of the n th band. $\Delta\mu_{0n}$ is obtained within Liptay's adiabatic treatment (ref 34) from the second-order derivative coefficient of the $\Delta\epsilon(\nu)$ spectrum analysis and is multiplied by the local field correction $f_{int} = 1.33$. The experimental μ_{0n} and $\Delta\mu_{0n}$ values, and therefore the β_{0n} contributions, are unsigned.

vertical excitation energies without anions, and the low-energy bands also correlate less good with the experimental trends. In summary, the calculations reproduce qualitatively the evolution of the excitation energies for the high-energy band but not for the low-energy one, while the average deviation with respect to the experimental results is smaller for the latter.

Calculations also reveal that the amplitude of the dipole moment increases upon excitation, that this increase is stronger for the low-energy state (called state 1) than for the high-energy one (called state 2), and that their amplitudes evolve monotonically from compound 1 to 5 (Table 4). Since the molecules are charged, the dipole moments depend on the origin of the Cartesian axes (here the center of mass) but the $\Delta\mu$ values do not. The CI density results are in close agreement to the FF TDDFT values when (i) the non-equilibrium solvation model is employed and when (ii) ground state geometries have been optimized accounting for the solvent effects with IEFPCM. When adopting the equilibrium solvation model for the excited state, CI density dipole moments differ from the corresponding non-equilibrium results, in particular for μ_2 . Further differences appear when considering the excited state optimized geometries and the equilibrium solvation

model. These latter values have been calculated to make a comparison with the $\Delta\mu$ values extracted from the Stark experimental data of refs 4g, 4j, and 4k. Contrasted agreement between theory and experiment is observed with overestimations of $\Delta\mu_1$ (especially for 5) and underestimations of $\Delta\mu_2$ (especially 3 and 4). This comparison should however not be pushed too far, owing to the particular experimental conditions used to carry out SS measurements.

III.D. SOS Analysis of the First Hyperpolarizabilities.

Several approximations were employed to calculate the first hyperpolarizabilities and to rationalize their evolutions as a function of the size and the nature of the ligands. First, the SOS scheme limited to one or two excited states is employed to analyze the dominant diagonal (longitudinal) tensor component, and then, full calculations of the β tensors are performed using the TDDFT scheme. The SOS results are displayed in Table 5 and Figure 6. In general, the larger the conjugation length in 1–4, the larger the μ_{01} and μ_{02} values and the larger the $\Delta\mu_{01}$ and $\Delta\mu_{02}$ values, but the smaller the ΔE_{01} and ΔE_{02} values. In this respect, it is interesting to see that 4 presents larger μ_{01} and μ_{02} values than 5, and also smaller ΔE_{01} and ΔE_{02} but smaller $\Delta\mu_{01}$ and $\Delta\mu_{02}$, demonstrating that the concept of

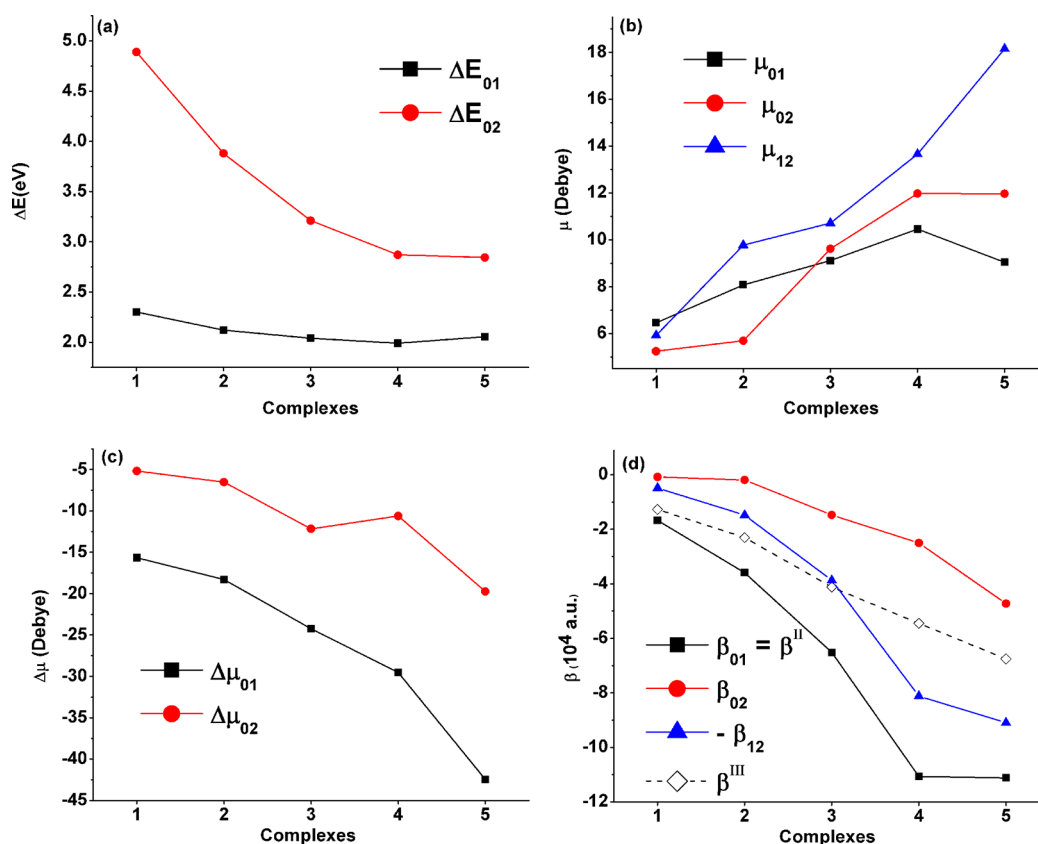


Figure 6. Excitation energies, transition dipole moments, dipole moment differences between the ground and excited states, and static first hyperpolarizabilities calculated using the two-state and three-state approximations. All calculations were performed at the TDDFT/B3P86 level of approximation (except for μ_{12} , see text) using the IEFPCM scheme (solvent = MeCN) on molecular structures optimized at the IEFPCM/DFT/B3P86 level.

conjugation length has different manifestations for different properties. The μ_{02} and ΔE_{02} quantities evolve similarly to the μ_{01} and ΔE_{01} values, though (i) μ_{02} gets larger than μ_{01} for $n > 1$ and (ii) ΔE_{02} remains larger than ΔE_{01} but it decreases faster with the ligand size. As a consequence, both β_{01} and β_{02} increase monotonically with n but the enhancement rate for β_{02} is stronger and the β_{02}/β_{01} ratio increases with n . Both contribute to the enhancement of the total first hyperpolarizability, since the $\Delta\mu$ along z are both negative, evidencing the global electron transfer from the Ru and its environment toward the pyridyl pyridinium ligand. These trends for the β_{01} and β_{02} contributions (and for the β_{02}/β_{01} ratios) can be related to the MLCT components of these excited states as described in the above section. This increase of β_{01} with the ligand size is also typical and associated with the extension of the π -conjugation length, as already evidenced in many systems encompassing organic D/A π -conjugated systems and those including metallic groups like the ferrocenyl moiety.^{4–8} Nevertheless, this monotonic increase of the calculated β_{01} in the $n = 0–3$ sequence differs from the experimental data derived from Stark spectroscopy where β_{01} decreases between $n = 2$ and $n = 3$, or is at least stabilized. Note that the β_{01} values evaluated from the theoretical spectroscopic data calculated by Coe et al. in ref 4k and reported in ref 8 are both in qualitative agreement with ours, demonstrating no sign of leveling off between $n = 2$ and $n = 3$.

β_{12} displays a very similar trend to β_{01} with an absolute value lying between those of β_{01} and β_{02} , but it reduces the amplitude of β since it is of opposite sign. Consequently, within the three-

state approximation (eq 5), the β^{III} values of 1–5 are in the ratio 1.00:1.81:3.24:4.29:5.31. These values are 20–50% smaller than those within the two-state approximation (eq 2), evidencing the limitations of that approximation due to not considering the contributions of the second excited state.

III.E. TDHF and TDDFT Investigations on the First Hyperpolarizabilities. In a second step, the HF and DFT response approaches, the TDHF and TDDFT methods, were employed to calculate the static and dynamic first hyperpolarizabilities and to rationalize their evolutions as a function of the size and of the nature of the ligands. The TDDFT scheme was applied in combination with the B3P86, M06, M06-2X, and LC-BLYP XC functionals. Like the SOS data discussed above, the calculated β_{zzz} ($\lambda = 1900$ nm) values (Table S6, Supporting Information) evidence also an increase from 1 to 4. However, the TDHF and TDDFT methods give smaller β_{zzz} for 5 than for 4, contrary to the SOS scheme limited to one or two excited states, evidencing therefore the role of the *other* excited states.

The calculated β_{HRS} values at 1900 nm displayed in Figure 7 also evidence an increase from 1 to 4 and then a decrease from 4 to 5. The trends for the calculated β_{HRS} are similar to those obtained for β_{zzz} , which is consistent with the one-dimensional nature of the complexes and the fact that β_{zzz} is the dominant tensor component. More data are given in Table S7 (Supporting Information). The one-dimensional nature of the Ru complexes is supported by the depolarization ratios close to 5.0.

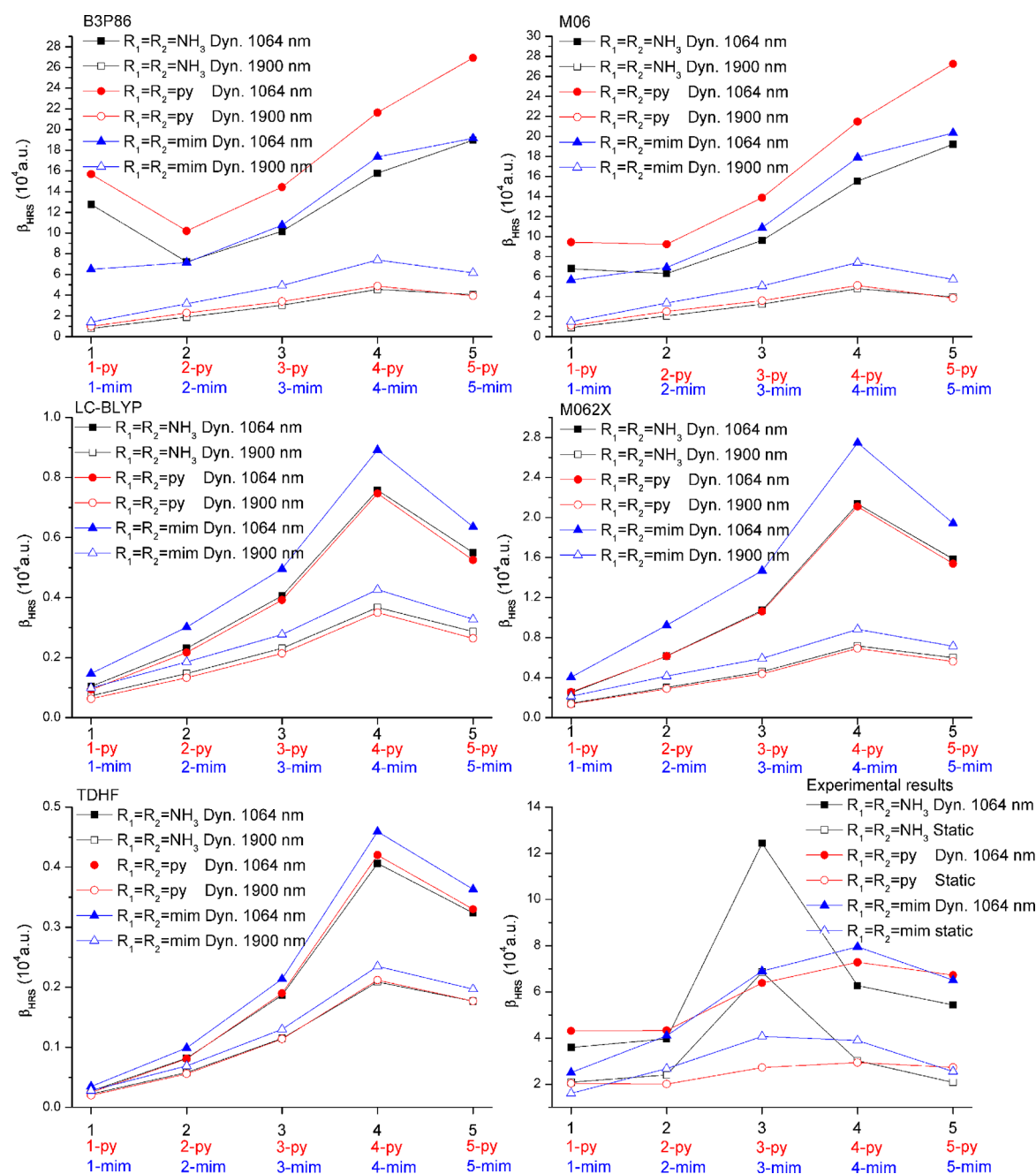


Figure 7. β_{HRS} responses (10 au , $\lambda = 1900$ and 1064 nm) calculated at different levels of approximation (TDHF and TDDFT with different XC functionals, with the LANL2DZ/6-31+G(d) basis set) in comparison with experimental HRS results (refs 4g, 4j, and 4k). The calculations are performed using the IEFPCM scheme (solvent = MeCN) on molecular structures optimized at the DFT/B3P86/(LANL2DZ, 6-31G*) level (*in vacuo*).

In the py- and mim-substituted complexes, no matter which calculation method is employed, the trends on the $\lambda = 1900 \text{ nm}$ first hyperpolarizabilities are the same as for the unsubstituted derivatives; i.e., they follow the order $1\text{-py(mim)} < 2\text{-py(mim)} < 3\text{-py(mim)} < 5\text{-py(mim)} < 4\text{-py(mim)}$. However, the description of the substitution effects is not completely independent of the method. Indeed, when using the B3P86 and M06 XC functionals, the trend is $x < x\text{-py} \ll x\text{-mim}$ ($x = 1, 2, 3, 4$), whereas with the LC-BLYP and M06-2X functionals as well as the TDHF method it becomes $x\text{-py} < x \ll x\text{-mim}$. Still, the β_{HRS} values are similar within 25% in the x and $x\text{-py}$ families of compounds, but this difference highlights the limitations of the predictive power of the TDDFT and TDHF approaches.

Using the experimental HRS values, the substituent leading to the largest β value differs as a function of the ligand size.

When considering a smaller wavelength ($\lambda = 1064 \text{ nm}$), the LC-BLYP, M06-2X, and TDHF methods provide the same trends with respect to the substitution and to the ligand size as those observed at 1900 nm . However, according to the B3P86 and M06 results, the hyperpolarizabilities decrease from 1 to 2 and from 1-py to 2-py and then increase up to 5 and 5-py, respectively. In the mim-substituted series, β_{HRS} increases from 1-mim to 5-mim. In addition, the py-substituted complexes have a larger β value than the unsubstituted and mim-substituted complexes. This distinct behavior is related to the fact that the second harmonic wavelength (532 nm) is beyond

the first dominant absorption band as calculated at the corresponding level of approximation. This is also visible from the data in Table S6 (Supporting Information) where the corresponding β_{zzz} values calculated with the B3P86 and M06 methods have opposite signs to those calculated with the LC-BLYP, M06-2X, and TDHF methods.

The relationships between the β_{HRS} values ($\lambda = 1900$ nm and $\lambda = 1064$ nm) calculated using different methods are assessed by performing linear regressions (Table S8, Supporting Information). At $\lambda = 1900$ nm, the B3P86 and M06 functionals provide very similar results (R^2 as large as 0.992 and slope of 0.958). There is also a nice consistency between the M06-2X and LC-BLYP functionals with $R^2 = 0.992$, though the slope is small (0.490). Besides two exceptions (B3P86-TDHF and M06-TDHF), the correlation is always excellent with $R^2 > 0.900$. These results indicate that all these functionals provide the same qualitative picture for the “static” and off-resonance first hyperpolarizabilities of ruthenium(II) ammine complexes. The β value ordering—associated with the slopes of the linear regressions—follows the nature of the XC functionals and in particular the amount of HF exchange.³⁵ B3P86 and M06, which contain, respectively, 20 and 27% of HF exchange, provide the largest β_{HRS} values; then come M06-2X with 54% and finally LC-BLYP with 100% HF exchange at the long-range. Finally, the TDHF values are smaller than the LC-BLYP results, evidencing the impact of electron correlation.

On the other hand, the first hyperpolarizabilities evaluated at $\lambda = 1064$ nm correspond to preresonant conditions only for the LC-BLYP and M06-2X XC functionals (and also at the TDHF level), whereas they are in resonance for the M06 and B3P86 XC functionals (the corresponding excitation energies are smaller; Table S5, Supporting Information). As a result, only a few correlations (among the LC-BLYP, M06-2X, and TDHF methods) remain good with $R^2 > 0.900$, while correlations between the other methods are poor. Also, the R^2 coefficient of the B3P86/M06 linear regression decreases to only 0.896 as a result of a substantial overestimation of the β_{HRS} value of the **1** and **1-py** complexes. When removing the data of these two complexes, the correlation gets better with $R^2 = 0.995$.

At the end of this section, the relationships between the experimental first hyperpolarizabilities at $\lambda = 1064$ nm and those calculated using the M06-2X and LC-BLYP methods are analyzed by performing linear regressions. As displayed in Figure 7, the experimentally obtained β_{HRS} for both the py- and mim-substituted complexes increase first from **1-py** (**1-mim**) to **4-py** (**4-mim**) and then decrease from **4-py** (**4-mim**) to **5-py** (**5-mim**). The calculated β_{HRS} for both the py- and mim-substituted complexes using both LC-BLYP and M06-2X methods exhibit the same trends as the experimental results. The linear regressions between the experimental and both M06-2X and LC-BLYP methods for the py- and mim-substituted complexes are good with $R^2 > 0.870$. However, for the unsubstituted complexes **1**–**5**, the corresponding linear regressions are poor with $R^2 < 0.090$. The reason is associated with the experimental β_{HRS} of **3**, which is significantly larger from those of the other complexes. On the other hand, when removing the data of **3**, the correlation gets much better with $R^2 = 0.996$ and 0.997 for the M06-2X and LC-BLYP XC functionals, respectively. Considering the linear regression obtained with complexes **1**, **2**, **4**, and **5**, a consistent experimental β_{HRS} value for **3** is assumed to amount to $(47 \pm 1) \times 10^3$ au, about one-third of the experimental data of Coe et al.^{4j,k}

IV. FURTHER DISCUSSION AND CONCLUSION

Extensive first principles calculations of the linear and nonlinear optical properties have been carried out for three series of one-dimensional ruthenium(II) ammine complexes having π -conjugated linkers of different size and nature. The substitution effects upon introducing one pyridine or one *N*-methylimidazole moiety as donor instead of ammonia have also been studied in detail. As discussed, these compounds are challenging for theoretical chemistry, whereas they constitute a class of molecules of high interest for nonlinear optics. Different XC functionals have been employed to characterize their geometries, electronic structures, excited state, and NLO properties. The solvent effects have been described within the IEF-PCM approach. In most of the cases, qualitative and even semiquantitative agreement has been observed between theory and experiment. When not the case, this was explained by resorting to the complexity of the experimental measurements and treatments (e.g., resonance effects) or to the limitations of the methods of calculations (approximate treatment of electron correlation in TDDFT). Notwithstanding this, calculations enable to get a deep insight into the structure/property relationships of these molecules as summarized below.

Two major types of methods have been employed to calculate and analyze the first hyperpolarizabilities: (i) the SOS scheme, applied to calculate the longitudinal β_{zzz} tensor component, truncated to one or two dominant excited states, of which the results are compared to Stark spectroscopy data and (ii) the quadratic response schemes, providing the whole SHG response of the compound, which can be compared to the values derived from HRS measurements. First, within both the two- and three-state (one or two excited states) approximation, TDDFT/B3P86 calculations predict that β increases monotonically from **1** to **4**. These TSA results are in good agreement with the TSA calculations by Inerbaev et al.⁸ but not completely with the theoretical results of Coe et al.^{4k} In detail, the calculated β values of Coe et al.^{4k} for the **1**–**4** complexes follow the $2 < 1 < 4 < 3$ order for ΔE_{01} , the $1 < 2 < 3 < 4$ order for μ_{01} , and the $4 < 1 < 2 < 3$ order for $\Delta\mu_{01}$, while according to the work of Inerbaev⁸ and the present work all the excitation energies decrease from **1** to **4** and both μ_{01} and $\Delta\mu_{01}$ increase from **1** to **4**. Part of these differences is attributed to the assumption of C_s symmetry in ref 4k. Interestingly, the β^{II} values calculated from the theoretical spectroscopic data reported by Coe et al. follow the $1 < 2 < 3 < 4$ ordering in line with both the calculations of Inerbaev⁸ and of the present work. On the other hand, all calculations differ from the “experimental” β^{II} values calculated using experimental spectroscopic quantities, which for **1**–**4** are in the ratio 1.00:1.46:4.02:3.96 ($\beta_0[S]$ in Table 3 of ref 4k), since in that case β decreases from **3** to **4** or at least levels off, considering experimental precision. This difference in β^{II} values has been traced to the differences in the ΔE_{01} and μ_{01} values of complexes **3**–**4**: experimentally,^{4k} $\Delta E_{01}(\mathbf{3}) < \Delta E_{01}(\mathbf{4})$ and, in magnitude, $\mu_{01}(\mathbf{4}) < \mu_{01}(\mathbf{3})$, whereas calculations predict the opposite (Table 5). Calculations of β^{III} values have then recalled the importance of the other excited states for describing the second-order NLO response of these Ru(II) complexes: the β_{02} contribution is small but increases fast with the ligand size, whereas the off-diagonal β_{12} term is much larger than β_{02} and is of opposite sign to both β_{01} and β_{02} so that the β^{III} values are significantly smaller than the β^{II} ones.

Another difference between theory and experiment concerns the relative β^{II} values of compounds **4** and **5** where experiment predicts β^{II} of **5** to be about 20% smaller than that of **4**, whereas calculations predict very similar values. In this case, the difference is traced back to a larger theoretical $\Delta\mu_{01}$ value for **4**. The relative β values of **4** and **5** change little when accounting for a second excited state (β_{02} and β_{12} terms), but the contributions of all the other excited states are such that in the nonresonant frequency regime $\beta(\mathbf{4}) > \beta(\mathbf{5})$ (Tables S6 and S7, Supporting Information). This points out the limitations of the two-state approximation—independently whether the spectroscopic quantities are obtained from measurements or calculations—to interpret the variations in first hyperpolarizabilities of compounds containing too different ligands.

Second, off-resonant ($\lambda = 1900$ nm) β_{HRS} values calculated at the TDDFT or TDHF levels show again a monotonic increase in the **1–4** series but a decrease between **4** and **5**. Similar trends are observed for the py-substituted and mim-substituted species. These calculations have evidenced the dominance of the β_{zzz} tensor components, which matches the depolarization ratio values close to 5.0. When the calculations are performed for a wavelength of 1064 nm, β increases substantially, especially with the B3P86, M06, and M06-2X XC functionals, since the second-harmonic wavelength (532 nm) is very close to the excitation energies. Still, β_{HRS} displays the same monotonic increasing behavior from **1** to **4**, from **1-py** to **4-py**, and from **1-mim** to **4-mim**. Besides the result of compound **3**, these data are in close agreement with the experimental results obtained at $\lambda = 1064$ nm, including the fact that $\beta_{\text{HRS}}(\mathbf{1-py}) < \beta_{\text{HRS}}(\mathbf{2-py}) < \beta_{\text{HRS}}(\mathbf{3-py}) < \beta_{\text{HRS}}(\mathbf{4-py})$ and $\beta_{\text{HRS}}(\mathbf{1-mim}) < \beta_{\text{HRS}}(\mathbf{2-mim}) < \beta_{\text{HRS}}(\mathbf{3-mim}) < \beta_{\text{HRS}}(\mathbf{4-mim})$. However, there remains a difference between theory and experiment in the sense that the saturation of β versus n is clearly visible for the measured quantities but not for the calculations. It is difficult to go further in this analysis, since the resonance effects have a strong impact on the β responses and therefore since the conventional TSA presents severe limitations, for instance, due to the lack of damping, the lack of vibronic structure, and the missing higher-energy states.³⁶

The substitution of the ammonia group opposite to the conjugated ligand by pyridine and especially by *N*-methylimidazole has been analyzed and found to lead to (i) changes in the geometry, (ii) displacements of the orbital energy levels (mostly the HOMO), (iii) variations in the orbital composition (the py and mim moieties contribute to the HOMO), (iv) shifts of the absorption bands (to the red in the case of mim substitution), and (v) variations of the first hyperpolarizability. In particular, calculations substantiate the fact that the NH_3 -to-(*N*-methylimidazole) substitution enhances the first hyperpolarizability by about 25%.

Besides their analysis in terms of linear optical properties via the SOS expression, the second-order NLO responses have been interpreted as a function of the structural and electronic properties. In particular, we have observed that, upon increasing the ligand size, (i) the Ru–N²(NH₃) coordination bond length increases, (ii) the Ru–N⁷(ligand) bond as well as the other Ru–N(NH₃) bonds shorten, (iii) the bond length alternation (BLA) of the linker between the two pyridine rings decreases, (iv) both the HOMO and LUMO levels shift upward, (v) the contribution from the Ru orbitals in the HOMO decreases, and (vi) the MLCT character decreases for the first excited state while it increases for the second.

In the future, we aim at extending our investigation of this interesting class of compounds by considering two-dimensional and three-dimensional Ru(II) complexes as well as other substituents.

■ ASSOCIATED CONTENT

● Supporting Information

Comparison between molecular structures optimized with different XC functionals and the experimental single crystal data; complete ref 32; convergence of the calculated differences of dipole moments between the ground and excited states using FF calculations with the added field along the *z* direction; TDDFT/B3P86 excitation energies (nm) and oscillator strengths of all the complexes; comparison between ground state and excited state geometry for complexes **1–4**; optimized molecular structures, TDDFT/B3P86 excitation energies, oscillator strengths, and transition nature for complexes **1–5** with three surrounding [PF₆][−] anions; calculated excitation energy and oscillator strengths with different XC functionals for complexes **1–4**; β_{zzz} and β_{HRS} values of compounds **1–5** calculated at different levels of approximation in comparison with experiment; and relationships between the first hyperpolarizabilities calculated at different levels of approximation as well as the experimental results. This material is available free of charge via the Internet at <http://pubs.acs.org>.

■ AUTHOR INFORMATION

Corresponding Author

*E-mail: benoit.champagne@fundp.ac.be.

Notes

The authors declare no competing financial interest.

■ ACKNOWLEDGMENTS

We gratefully acknowledge the financial support of the Fonds Spéciaux de Recherche of the Académie universitaire Louvain (AUL) cofunded by the Marie Curie Actions of the European Commission (ADi/DB/986.2011). This work is also supported by funds from the AUL (ARC “Extended- π Conjugated Molecular Tinkertoys for optoelectronics and spintronics”) and by the Belgian Government (IUAP No P7/5 “Functional Supramolecular Systems”). The calculations were performed on the Interuniversity Scientific Computing Facility (ISCF) installed at the Facultés Universitaires Notre-Dame de la Paix (Namur, Belgium), for which we gratefully acknowledge financial support of the FNRS-FRFC (Convention Nos. 2.4.617.07.F and 2.5020.11), and of the FUNDP.

■ REFERENCES

- (1) (a) *Nonlinear Optical Properties of Organic Molecules and Crystals*; Chemla, D. S., Zyss, J., Eds.; Academic Press: Orlando, FL, 1987; Vols. 1 and 2. (b) *Molecular Nonlinear Optics: Materials, Physics and Devices*; Zyss, J., Ed.; Academic Press: Boston, MA, 1994. (c) *Organic Nonlinear Optical Materials*; Bosshard, Ch., Sutter, K., Prêtre, Ph., Hulliger, J., Flörshemer, M., Kaatz, P., Günter, P., Eds.; Advances in Nonlinear Optics, Vol. 1; Gordon & Breach: Amsterdam, The Netherlands, 1995. (d) *Nonlinear Optics of Organic Molecules and Polymers*; Nalwa, H. S., Miyata, S., Eds.; CRC Press: Boca Raton, FL, 1997. (e) *Nonlinear Optical Properties of Matter: From Molecules to Condensed Phases*; Papadopoulos, M. G., Leszczynski, J., Sadlej, A. J., Eds.; Springer: Dordrecht, The Netherlands, 2006.
- (2) (a) Nalwa, H. S. *Appl. Organomet. Chem.* **1991**, *5*, 349–377. (b) Marder, S. R. In *Inorganic Materials*, 2nd ed.; Bruce, D. W., O'Hare, D., Eds.; Wiley: Chichester, U.K., 1992; pp 121–169. (c) Kanis, D. R.; Ratner, M. A.; Marks, T. J. *Chem. Rev.* **1994**, *94*, 195–

242. (d) Stephenson, G. R. *Annu. Rep. Prog. Chem., Sect. B: Org. Chem.* **1994**, *91*, 251–288. (e) Long, N. J. *Angew. Chem., Int. Ed. Engl.* **1995**, *34*, 21–38. (f) Osella, D.; Milone, L.; Nervi, C.; Ravera, M. J. *Organomet. Chem.* **1995**, *488*, 1–7. (g) Verbiest, T.; Houbrechts, S.; Kauranen, M.; Clays, C.; Persoons, A. *J. Mater. Chem.* **1997**, *7*, 2175–2189. (h) Zhang, L.; Ding, F.; Zhao, K.; Yang, L.; Wang, C.; Li, L. *Hecheng Huaxue* **1997**, *5*, 17–27. (i) Whittall, I. R.; McDonagh, A. M.; Humphrey, M. G.; Samoc, M. *Adv. Organomet. Chem.* **1998**, *42*, 291–362. (j) Whittall, I. R.; McDonagh, A. M.; Humphrey, M. G.; Samoc, M. *Adv. Organomet. Chem.* **1998**, *43*, 349–405. (k) Heck, J.; Dabek, S.; Meyer-Friedrichsen, T.; Wong, H. *Coord. Chem. Rev.* **1999**, *190*–192, 1217–1254. (l) Gray, G. M.; Lawson, C. M. In *Optoelectronic Properties of Inorganic Compounds*; Roundhill, D. M., Fackler, J. P., Jr., Eds.; Plenum: New York, 1999; pp 1–27. (m) Shi, S. In *Optoelectronic Properties of Inorganic Compounds*; Roundhill, D. M., Fackler, J. P., Jr., Eds.; Plenum: New York, 1999; pp 55–105. (n) Yamashita, M.; Manabe, T.; Kawashima, T.; Shimizu, H. *Trends Chem. Phys.* **1999**, *7*, 1–33. (o) Yam, V. W.-W.; Lo, K. K. W.; Wong, K. M. C. *J. Organomet. Chem.* **1999**, *578*, 3–30. (p) Di Bella, S. *Chem. Soc. Rev.* **2001**, *30*, 355–366. (q) Coe, B. J. In *Comprehensive Coordination Chemistry II*; McCleverty, J. A., Meyer, T. J., Eds.; Pergamon Press: Oxford, U.K., 2004; Vol. 9, pp 621–687. (r) Clays, K. *NATO Sci. Ser.* **2004**, *165*, 379–393. (s) Boss, S. R.; Wheatley, A. E. H. *Organomet. Chem.* **2005**, *32*, 39–60. (t) Cariati, E.; Pizzotti, M.; Roberto, D.; Tessore, F.; Ugo, R. *Coord. Chem. Rev.* **2006**, *250*, 1210–1233. (u) Di Bella, S.; Dragonetti, C.; Pizzotti, M.; Roberto, D.; Tessore, F.; Ugo, R. *Top. Organomet. Chem.* **2010**, *28*, 1–55. (v) Humphrey, M. G.; Cifuentes, M. P.; Samoc, M. *Top. Organomet. Chem.* **2010**, *28*, 57–73. (w) Garcia, M. H.; Florindo, P. In *Organometallic Compounds: Preparation, Structure and Properties*; Chin, H. F., Ed.; Nova Science Publishers: 2010; pp 347–372. (x) Manzur, C.; Fuentealba, M.; Hamon, J.-R.; Carrillo, D. *Coord. Chem. Rev.* **2010**, *254*, 765–780.
- (3) (a) Calabrese, J. C.; Cheng, L.-T.; Green, J. C.; Marder, S. R.; Tam, W. J. *Am. Chem. Soc.* **1991**, *113*, 7227–7232. (b) Verbiest, T.; Houbrechts, S.; Kauranen, M.; Clays, K.; Persoons, A. *J. Mater. Chem.* **1997**, *7*, 2175–2189. (c) Nalwa, H. S.; Watanabe, T.; Miyata, S. In *Nonlinear Optics of Organic Molecules and Polymers*; Nalwa, H. S., Miyata, S., Eds.; CRC Press: 1997; pp 89–350. (d) Nalwa, H. S. In *Nonlinear Optics of Organic Molecules and Polymers*; Nalwa, H. S., Miyata, S., Eds.; CRC Press: 1997; pp 611–797. (e) Zhang, H.; Wang, X.; Zhang, K.; Teo, B. K. *Coord. Chem. Rev.* **1999**, *183*, 157–195. (f) Qin, J.; Liu, D.; Dai, C.; Chen, C.; Wu, B.; Yang, C.; Zhan, C. *Coord. Chem. Rev.* **1999**, *188*, 23–34. (g) Wolff, J. J.; Wortmann, R. *Adv. Phys. Org. Chem.* **1999**, *32*, 121–217. (h) Topaloglu, I. *J. Fac. Sci. Ege Univ.* **1999**, *22*, 41–55. (i) Le Bozec, H.; Renouard, T. *Eur. J. Inorg. Chem.* **2000**, 229–239. (j) Long, N. J. In *Optoelectronic Properties of Inorganic Compounds*; Roundhill, D. M., Fackler, J. P., Jr., Eds.; Plenum: New York, 1999; pp 107–167. (k) Barlow, S.; Marder, S. R. *Chem. Commun.* **2000**, 1555–1562. (l) Goovaerts, E.; Wenseleers, W. E.; Garcia, M. H.; Cross, G. H. In *Handbook of Advanced Electronic and Photonic Materials and Devices*; Nalwa, H. S., Ed.; Elsevier Inc.: 2001; Vol. 9, pp 127–191. (m) Houbrechts, S.; Hendrickx, E.; Verbiest, T.; Clays, K.; Persoons, A. In *Electron transfer in chemistry*; Balzani, V., Ed.; Wiley-VCH: 2001; Vol. 5, pp 243–281. (n) Peris, E. *Coord. Chem. Rev.* **2004**, *248*, 279–297. (o) Cifuentes, M. P.; Humphrey, M. G. *J. Organomet. Chem.* **2004**, *689*, 3968–3981. (p) Wong, W.-Y. *Comments Inorg. Chem.* **2005**, *26*, 39–74. (q) Asselberghs, I.; Therien, M. J.; Coe, B. J.; McCleverty, J. A.; Clays, K. *ACS Symp. Ser.* **2006**, *928*, 527–540. (r) Clays, K.; et al. In *Linear and Nonlinear Optics of Organic Materials VII*; Nunzi, J. M., Ed.; Proceedings of SPIE, Vol. 6653; SPIE: 2007; pp 1–258. (s) Morrall, J. P.; Dalton, G. T.; Humphrey, M. G.; Samoc, M. *Adv. Organomet. Chem.* **2008**, *55*, 61–136. (t) Maury, O.; le Bozec, H. In *Molecular Materials*; Bruce, D. W., O'Hare, D., Walton, R. I., Eds.; John Wiley & Sons, Inc.: 2010; pp 1–59. (u) Li, L.; Hou, H. In *Organometallic Compounds: Preparation, Structure and Properties*; Chin, H. F., Ed.; Nova Science Publishers: 2010; pp 115–158.
- (4) (a) Coe, B. J.; Chamberlain, M. C.; Essex-Lopresti, J. P.; Gaines, S.; Jeffery, J. C.; Houbrechts, S.; Persoons, A. *Inorg. Chem.* **1997**, *36*, 3284–3292. (b) Coe, B. J.; Essex-Lopresti, J. P.; Harris, J. A.; Houbrechts, S.; Persoons, A. *Chem. Commun.* **1997**, 1645–1646. (c) Coe, B. J.; Harris, J. A.; Harrington, L. J.; Jeffery, J. C.; Rees, L. H.; Houbrechts, S.; Persoons, A. *Inorg. Chem.* **1998**, *37*, 3391–3399. (d) Coe, B. J.; Harris, J. A.; Asselberghs, I.; Persoons, A.; Jeffery, J. C.; Rees, L. H.; Gelbrich, T.; Hursthouse, M. B. *J. Chem. Soc., Dalton Trans.* **1999**, 3617–3625. (e) Houbrechts, S.; Asselberghs, I.; Persoons, A. P.; Coe, B. J.; Harris, J. A.; Harrington, L. J.; Chamberlain, M. C.; Essex-Lopresti, J. P.; Gaines, S. *Proc. SPIE* **1999**, *3796*, 209–218. (f) Coe, B. J.; Harris, J. A.; Clays, K.; Persoons, A.; Wostyn, K.; Brunchwitz, B. S. *Chem. Commun.* **2001**, 1548–1549. (g) Coe, B. J.; Harris, J. A.; Brunchwitz, B. S. *J. Phys. Chem. A* **2002**, *106*, 897–905. (h) Coe, B. J.; Jones, L. A.; Harris, J. A.; Sanderson, E. E.; Brunchwitz, B. S.; Asselberghs, I.; Clays, K.; Persoons, A. *Dalton Trans.* **2003**, 2335–2341. (i) Harris, J. A.; Coe, B. J.; Jones, L. A.; Brunchwitz, B. S.; Asselberghs, I.; Clays, K.; Persoons, A. *P. Proc. SPIE* **2003**, *5212*, 341–350. (j) Coe, B. J.; Jones, L. A.; Harris, J. A.; Brunchwitz, B. S.; Asselberghs, I.; Clays, K.; Persoons, A. *J. Am. Chem. Soc.* **2003**, *125*, 862–863. (k) Coe, B. J.; Jones, L. A.; Harris, J. A.; Brunchwitz, B. S.; Asselberghs, I.; Clays, K.; Persoons, A.; Garin, J.; Orduna, J. *J. Am. Chem. Soc.* **2004**, *126*, 3880–3891. (l) Coe, B. J.; Harris, J. A.; Brunchwitz, B. S.; Garin, J.; Orduna, J.; Coles, S. J.; Hursthouse, M. B. *J. Am. Chem. Soc.* **2004**, *126*, 10418–10427. (m) Coe, B. J.; Harries, J. L.; Helliwell, M.; Brunchwitz, B. S.; Harris, J. A.; Asselberghs, I.; Hung, S.-T.; Clays, K.; Horton, P. N.; Hursthouse, M. B. *Inorg. Chem.* **2006**, *45*, 1215–1227. (n) Coe, B. J.; Harries, J. L.; Harris, J. A.; Brunchwitz, B. S.; Horton, P. N.; Hursthouse, M. B. *Inorg. Chem.* **2006**, *45*, 11019–11029. (o) Coe, B. J.; Harries, J. L.; Helliwell, M.; Jones, L. A.; Asselberghs, I.; Clays, K.; Brunchwitz, B. S.; Harris, J. A.; Garin, J.; Orduna, J. *J. Am. Chem. Soc.* **2006**, *128*, 12192–12204.
- (5) (a) Coe, B. J.; Harris, J. A.; Jones, L. A.; Brunchwitz, B. S.; Song, K.; Clays, K.; Garin, J.; Orduna, J.; Coles, S. J.; Hursthouse, M. B. *J. Am. Chem. Soc.* **2005**, *127*, 4845–4859. (b) Swanson, C. E.; Coe, B. J.; Helliwell, M.; Harris, J. A.; Brunchwitz, B. B.; Hursthouse, M. B.; Horton, P. N. Abstracts of Papers, 234th ACS National Meeting, Boston, MA, Aug 19–23, 2007, INOR-581. (c) Coe, B. J.; Foxon, S. P.; Harper, E. C.; Helliwell, M.; Raftery, J.; Swanson, C. A.; Brunchwitz, B. S.; Clays, K.; Franz, E.; Garin, J.; et al. *J. Am. Chem. Soc.* **2010**, *132*, 1706–1723. (d) Coe, B. J.; Fielden, J.; Foxon, S. P.; Asselberghs, I.; Clays, K.; Brunchwitz, B. S. *Inorg. Chem.* **2010**, *49*, 10718–10726.
- (6) Coe, B. J.; Harris, J. A.; Brunchwitz, B. S.; Asselberghs, I.; Clays, K.; Garin, J.; Orduna, J. *J. Am. Chem. Soc.* **2005**, *127*, 13399–13410.
- (7) (a) Coe, B. J.; Houbrechts, S.; Asselberghs, I.; Persoons, A. *Angew. Chem., Int. Ed.* **1999**, *38*, 366–369. (b) Coe, B. J. *Chem.—Eur. J.* **1999**, *5*, 2464–2471. (c) Harries, J. L.; Coe, B. J.; Harris, J. A.; Brunchwitz, B. S.; Clays, K.; Asselberghs, I. Abstracts of Papers, 230th ACS National Meeting, Washington, DC, Aug 28–Sept 1, 2005, INOR-312. (d) Boubekur-Lecaque, L.; Coe, B. J.; Clays, K.; Foerier, S.; Verbiest, T.; Asselberghs, I. *J. Am. Chem. Soc.* **2008**, *130*, 3286–3287. (e) Boubekur-Lecaque, L.; Coe, B. J.; Harris, J. A.; Helliwell, M.; Asselberghs, I.; Clays, K.; Foerier, S.; Verbiest, T. *Inorg. Chem.* **2011**, *50*, 12886–12899.
- (8) Inerbaev, T. M.; Belosludov, R. V.; Mizuseki, H.; Takahashi, M.; Kawazoe, Y. *J. Chem. Theory Comput.* **2006**, *2*, 1325–1334.
- (9) (a) Perdew, J. P. *Phys. Rev. B* **1986**, *33*, 8822–8824. (b) Becke, A. D. *J. Chem. Phys.* **1993**, *98*, 5648–5652.
- (10) Wadt, W. R.; Hay, P. J. *J. Chem. Phys.* **1985**, *82*, 284–298.
- (11) (a) Becke, A. D. *J. Chem. Phys.* **1993**, *98*, 1372–1377. (b) Lee, C.; Yang, W.; Parr, R. G. *Phys. Rev. B* **1988**, *37*, 785–789.
- (12) (a) Perdew, J. P.; Burke, K.; Ernzerhof, M. *Phys. Rev. Lett.* **1996**, *77*, 3865–3868. (b) Perdew, J. P.; Burke, K.; Ernzerhof, M. *Phys. Rev. Lett.* **1997**, *78*, 1396–1396.
- (13) (a) Becke, A. D. *Phys. Rev. A* **1988**, *38*, 3098–3100. (b) Miehlich, B.; Savin, A.; Stoll, H.; Preuss, H. *Chem. Phys. Lett.* **1989**, *157*, 200–206.
- (14) (a) Perdew, J. P.; Chevary, J. A.; Vosko, S. H.; Jackson, K. A.; Pederson, M. R.; Singh, D. J.; Fiolhais, C. *Phys. Rev. B* **1992**, *46*, 6671–

6687. (b) Perdew, J. P.; Burke, K.; Wang, Y. *Phys. Rev. B* **1996**, *54*, 16533–16539.
- (15) (a) Tao, J.; Perdew, J. P.; Staroverov, V. N.; Scuseria, G. E. *Phys. Rev. Lett.* **2003**, *91*, 146401/1–146401/4. (b) Staroverov, V. N.; Scuseria, G. E.; Tao, J.; Perdew, J. P. *J. Chem. Phys.* **2003**, *119*, 12129–12137.
- (16) (a) Zhao, Y.; Truhlar, D. G. *J. Chem. Phys.* **2006**, *125*, 194101/1–194101/18. (b) Zhao, Y.; Truhlar, D. G. *J. Phys. Chem. A* **2006**, *110*, 5121–5129. (c) Zhao, Y.; Truhlar, D. G. *Theor. Chem. Acc.* **2008**, *120*, 215–241.
- (17) See the Supporting Information for the comparison of molecular structures calculated with different XC functionals and the experimental single crystal data.
- (18) (a) Cancès, E.; Mennucci, B.; Tomasi, J. *J. Chem. Phys.* **1997**, *107*, 3032–3041. (b) Mennucci, B.; Cancès, E.; Tomasi, J. *J. Phys. Chem. B* **1997**, *101*, 10506–10517. (c) Cammi, R.; Mennucci, B.; Tomasi, J. *J. Chem. Phys.* **1999**, *110*, 7627–7638. (d) Tomasi, J.; Mennucci, B.; Cammi, R. *Chem. Rev.* **2005**, *105*, 2999–3093.
- (19) (a) van Gisbergen, S. J. A.; Rosa, A.; Ricciardi, G.; Baerends, E. J. *J. Chem. Phys.* **1999**, *111*, 2499–2506. (b) Sundholm, D. *Chem. Phys. Lett.* **1999**, *302*, 480–484. (c) Boulet, P.; Chermette, H.; Daul, C.; Gillardoni, F.; Rogemond, F.; Weber, J.; Zuber, G. *J. Phys. Chem. A* **2005**, *105*, 885–894. (d) Cavillot, V.; Champagne, B. *Chem. Phys. Lett.* **2002**, *354*, 449–457. (e) Atsumi, M.; González, L.; Daniel, C. *J. Photochem. Photobiol., A* **2007**, *190*, 310–320. (f) Alary, F.; Boggio-Pasqua, M.; Heully, J. L.; Marsden, C. J.; Vicendo, P. *Inorg. Chem.* **2008**, *47*, 5259–5266. (g) Herrmann, C.; Neugebauer, J.; Presselt, M.; Uhlemann, U.; Schmitt, M.; Rau, S.; Popp, J.; Reiher, M. *J. Phys. Chem. B* **2007**, *111*, 6078–6987. (h) Guthmüller, J.; Champagne, B.; Moucheron, C.; Kirsch-De Mesmaeker, A. *J. Phys. Chem. B* **2010**, *114*, 511–520.
- (20) Zhao, Y.; Truhlar, D. G. *J. Phys. Chem. A* **2006**, *110*, 5121–5129.
- (21) Adamo, C.; Barone, V. *J. Chem. Phys.* **1999**, *110*, 6158–6169.
- (22) Iikura, H.; Tsuneda, T.; Yanai, T.; Hirao, K. *J. Chem. Phys.* **2001**, *115*, 3540–3544.
- (23) (a) Sekino, H.; Bartlett, R. J. *J. Chem. Phys.* **1986**, *85*, 976–989. (b) Karna, S. P.; Dupuis, M. *J. Comput. Chem.* **1991**, *12*, 487–504.
- (24) (a) Runge, E.; Gross, E. K. U. *Phys. Rev. Lett.* **1984**, *52*, 997–1000. (b) van Gisbergen, S. J. A.; Snijders, J. G.; Baerends, E. J. *J. Chem. Phys.* **1998**, *109*, 10657–10668. (c) Thorvaldsen, A. J.; Ruud, K.; Kristensen, K.; Jørgensen, P.; Coriani, S. *J. Chem. Phys.* **2008**, *129*, 214108/1–214108/27.
- (25) (a) Cammi, R.; Cossi, M.; Tomasi, J. *J. Chem. Phys.* **1996**, *104*, 4611–4620. (b) Cammi, R.; Cossi, M.; Mennucci, B.; Tomasi, J. *J. Chem. Phys.* **1996**, *105*, 10556–10564. (c) Mennucci, B.; Cancès, E.; Tomasi, J. *J. Phys. Chem. A* **1997**, *101*, 10506–10517. (d) Mennucci, B.; Amovilli, C.; Tomasi, J. *Chem. Phys. Lett.* **1998**, *286*, 221–225.
- (26) (a) Oudar, J. L.; Chemla, D. S. *J. Chem. Phys.* **1977**, *66*, 2664–2668. (b) Oudar, J. L. *J. Chem. Phys.* **1977**, *67*, 446–457.
- (27) (a) Bethe, H. A.; Salpeter, E. E. In *Quantum Mechanics of One and Two Electron Atoms*; Plenum: New York, 1977. (b) Kuzyk, M. G. *Phys. Rev. Lett.* **2000**, *85*, 1218–1221 *erratum* **2003**, *90*, 039902; *comment* **2005**, *95*, 109401.
- (28) De Mey, K.; Perez-Moreno, J.; Reeve, J. E.; Lopez-Duarte, I.; Boczarow, I.; Anderson, H. L.; Clays, K. *J. Phys. Chem. C* **2012**, *116*, 13781–13787.
- (29) Verbiest, T.; Clays, K.; Rodriguez, V. *Second-Order Nonlinear Optical Characterizations Techniques: An Introduction*; CRC Press: New York, 2009.
- (30) (a) Bogdan, E.; Plaquet, A.; Antonov, L.; Rodriguez, V.; Ducasse, L.; Champagne, B.; Castet, F. *J. Phys. Chem. C* **2010**, *114*, 12760–12768. (b) Castet, F.; Bogdan, E.; Plaquet, A.; Ducasse, L.; Champagne, B.; Rodriguez, V. *J. Chem. Phys.* **2012**, *136*, 024506/1–024506/15.
- (31) Willetts, A.; Rice, J. E.; Burland, D. M.; Shelton, D. P. *J. Chem. Phys.* **1992**, *97*, 7590–7599.
- (32) Frisch, M. J.; Trucks, G. W.; Schlegel, H. B.; Scuseria, G. E.; Robb, M. A.; Cheeseman, J. R.; Montgomery, J. A.; Vreven, T.; Kudin, K. N.; et al. *Gaussian 09*, revision A.02; Gaussian, Inc.: Wallingford, CT, 2009.
- (33) (a) Tozer, D. J.; Amos, R. D.; Handy, N. C.; Roos, B. O.; Serrano-Andres, L. *Mol. Phys.* **1999**, *97*, 859–868. (b) Fabian, J. *Theor. Chem. Acc.* **2001**, *106*, 199–217. (c) Dreuw, A.; Weisman, J. L.; Head-Gordon, M. *J. Chem. Phys.* **2003**, *119*, 2943–2946. (d) Tozer, D. J. *J. Chem. Phys.* **2003**, *119*, 12697–12699. (e) Liao, M.-S.; Lu, Y.; Scheiner, S. *J. Comput. Chem.* **2003**, *24*, 623–631. (f) Dreuw, A.; Head-Gordon, M. *J. Am. Chem. Soc.* **2004**, *126*, 4007–4016. (g) Gritsenko, O.; Baerends, E. J. *J. Chem. Phys.* **2004**, *121*, 655–660. (h) Hieringer, W.; Görling, A. *Chem. Phys. Lett.* **2006**, *419*, 557–562. (i) Magyar, R.; Tretiak, S. *J. Chem. Theory Comput.* **2007**, *3*, 976–987. (j) Aquino, A. J. A.; Nachtigallova, D.; Hobza, P.; Truhlar, D. G.; Hattig, C.; Lischka, H. *J. Comput. Chem.* **2011**, *32*, 1217–1227. (k) Escudero, D.; Gonzalez, L. *J. Chem. Theory Comput.* **2012**, *8*, 203–213.
- (34) (a) Labhart, H. *Adv. Chem. Phys.* **1967**, *13*, 179–204. (b) Liptay, W. In *Excited States*; Lim, E. C., Ed.; Academic Press: New York, 1974; Vol. 1, pp 129–229. (c) Baumann, W. In *Physical Methods of Chemistry*; Rossiter, B. W.; Hamilton, J. F., Eds.; Wiley: New York, 1989; Vol. IIIB, pp 45–131. (d) Baumann, W.; Nagy, Z.; Maiti, A. K.; Reis, H.; Rodrigues, S. V.; Detzer, N. In *Dynamics and Mechanism of Photoinduced Charge Transfer and Related Phenomena*; Mataga, N.; Okada, T.; Masuhara, H., Eds.; Elsevier: Amsterdam, The Netherlands, 1992; pp 211–229.
- (35) de Wergifosse, M.; Champagne, B. *J. Chem. Phys.* **2011**, *134*, 074113/1–074113/13.
- (36) (a) Mancois, F.; Pozzo, J. L.; Pan, J.; Adamietz, F.; Rodriguez, V.; Ducasse, L.; Castet, F.; Plaquet, A.; Champagne, B. *Chem.—Eur. J.* **2009**, *15*, 2560–2571. (b) Sergeyev, S.; Didier, D.; Boitsov, V.; Teshome, A.; Asselberghs, I.; Clays, K.; Vande Velde, C.; Plaquet, A.; Champagne, B. *Chem.—Eur. J.* **2010**, *16*, 8181–8190.